Journal of South American Earth Sciences 101 (2020) 102627

Contents lists available at ScienceDirect

Journal of South American Earth Sciences

journal homepage: www.elsevier.com/locate/jsames

Geochemical features of hydrothermal systems in Jujuy Province, Argentina: Hints for geothermal fluid exploration

Yésica Peralta Arnold[a,b,*], M. Gabriela Franco[a], Franco Tassi[c,d], Pablo J. Caffe[a,b], Cynthia B. Jofre[a,b], Marcelo Claros[b], Juan P. Villalba Ulberich[a,b], Andrea L. Rizzo[e], Jacopo Cabassi[c,d]

[a] Instituto de Ecorregiones Andinas (INECOA), Universidad Nacional de Jujuy-CONICET, Instituto de Geología y Minería, Av. Bolivia 1661, San Salvador de Jujuy, CP 4600, Jujuy, Argentina
[b] Facultad de Ingeniería, Universidad Nacional de Jujuy, Ítalo Palanca 10, 4600, San Salvador de Jujuy, Argentina
[c] University of Florence, Earth Science Department, Earth Sciences, Via La Pira 4, 50121, Florence, Italy
[d] CNR-IGG Institute of Geosciences and Earth Resources, Via La Pira 4, 50121, Firenze, Italy
[e] Istituto Nazionale di Geofisica e Vulcanologia (INGV), Sezione di Palermo, Via Ugo La Malfa 153, 90146, Palermo, Italy

ARTICLE INFO

Keywords:
Hydrothermal systems
Fluid geochemistry
Jujuy province
Geothermal resource

ABSTRACT

Fluid primary source(s) and chemical-physical processes controlling water and gas chemistry of thermal springs from Eastern Cordillera, sub-Andean Ranges and Santa Bárbara (Jujuy Province, northern Argentina) were investigated to provide information for a preliminary evaluation of the geothermal potential in these areas. Thermal manifestations in Eastern Cordillera (Reyes) and part of those in the western sector of sub-Andean Range (Aguas Calientes) are fed by shallow aquifers, interacting with Quaternary- Neogene rocks and the upper portion of Pliocene-Miocene formations (Orán Group), whereas the meteoric water recharge area is located at > 2500 m a.s.l., corresponding to Chañi hill. Differently, El Jordán thermal spring in the sub-Andean Range is fed by a hydrothermal aquifer hosted within highly porous and fractured formations of the Salta Group (Yacoraite Formation) and recharged by meteoric water from Sierra de Calilegua (~1500 m a.s.l.). The latter is the recharge area of the La Quinta geothermal waters as well, but these have been fed at higher altitudes (> 2500 m a.s.l.) in the range. The hydrothermal reservoir feeding the other thermal springs from the Santa Barbara system (Caimancito, El Palmar, and Siete Aguas) is recharged by meteoric water from Zapla Ranges and Santa Barbara Hill at < 2500 m a.s.l. The high-TDS (> 16,000 mg/L) Na^+-Cl^- La Quinta thermal springs are produced by interaction with the evaporite deposits of Salta Group, including halite, whereas the chemistry of El Palmar, El Jordán and Caimancito thermal springs, showing a Na^+-SO_4^{2-}(Cl^-) composition, depends on mixing with shallower SO_4^{2-}-rich waters interacting with gypsum deposits of Anta Formation. Dissolved and bubbling gases from all the investigated provinces are related to CO_2- and CH_4-rich crustal fluids produced by both thermogenic processes occurring within the hydrothermal systems and microbial activity at relatively low depth, with low to negligible mantle contribution, as indicated by the $^3He/^4He$ values ≤ 0.21 Ra. The fluid reservoir feeding the Quinta thermal springs shows the highest estimated temperatures (> 200 °C), which, considering the depth of Salta Group in the Santa Barbara system (~2000 m), support the idea, suggested by previous authors, of an anomalous geothermal gradient for this area, a promising pre-requisite for future exploitation of the geothermal resource.

1. Introduction

Argentine government has recently renewed the interest for geothermal energy (National Laws n. 26.190/06 and n. 27.191/15) and, overall, the exploitation of natural resources such as Li-rich deposits (Lopez Steinmetz, 2017). Encouraged by this pulse, geochemical investigations were recently carried out to describe the chemical and isotopic features of Tuzgle-Tocomar and Cerro Blanco hydrothermal fluids (Puna plateau) and Rosario de la Frontera, providing evidence for relatively high (≥200 °C and 130 °C, respectively) estimated reservoir

* Corresponding author. Instituto de Ecorregiones Andinas (INECOA), Universidad Nacional de Jujuy-CONICET, Instituto de Geología y Minería, Av. Bolivia 1661, San Salvador de Jujuy, CP 4600, Jujuy, Argentina.
E-mail address: yesicajael@gmail.com (Y. Peralta Arnold).

https://doi.org/10.1016/j.jsames.2020.102627
Received 6 February 2020; Received in revised form 24 April 2020; Accepted 27 April 2020
Available online 03 May 2020
0895-9811/

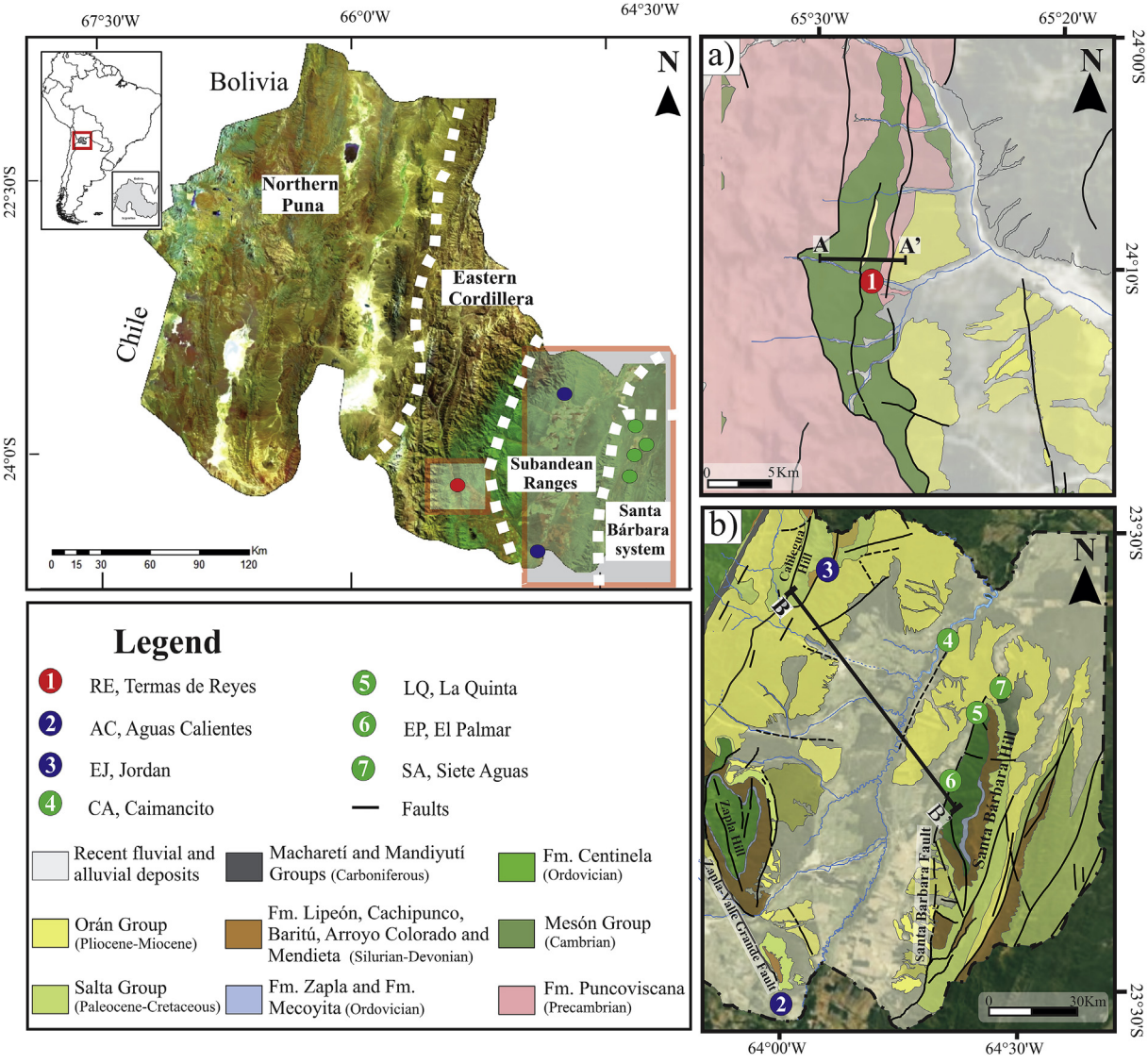

Fig. 1. Geographical map of Jujuy province showing the main geological domains; (a) Geological map of the Termas de Reyes area and location of thermal fluid discharges; (b) Geological map of sub- Andean Ranges and Santa Bárbara System and location of thermal fluid discharges. Geological maps were modified from Coira y Zappettini (2008).

temperatures (Giordano et al., 2016; Chiodi et al., 2015, 2019). Recently, Peralta Arnold et al. (2017) investigated the chemistry of thermal fluids from five zones in the northern Puna (Granada, Vilama, Pairique, Coranzuli and Olaroz; Jujuy Province) estimating reservoir temperatures of 150–200 °C. Notwithstanding the occurrence of a number of thermal manifestations in other areas of Jujuy Province represents promising geothermal resources, their chemical characteristics are poorly known. For these thermal springs only a few data (outlet temperatures and concentrations of the main solutes) were produced during geochemical surveys carried out in the 1970's and 1990's by different companies: 1) Aquater Ltd., with Jujuy Mining Direction and Mining Secretary (Aquater, 1980), 2) SA-Setec SRL-Cepic SC (Hidroproyectos et al., 1984), 3) Jujuy Government, Centro Regional de Energía Geotérmica (CREGEN, 1988). The present study aims to add information about the chemical and isotopic features of thermal fluids in Jujuy Province, focusing on thermal manifestations from 7 areas thoroughly investigated or with no previous data at all: Reyes, Aguas Calientes, El Jordán, Caimancito, El Palmar, La Quinta, and Siete Aguas (Fig. 1). The main target is to construct conceptual models to (i) describe the primary source(s) and chemical-physical processes controlling the compositional evolution of underground circulating fluids and (ii) provide hints for a preliminary evaluation of the geothermal potential of these hydrothermal systems.

2. Geologic regional setting

Four geological domains can be recognized in Jujuy Province according to distinct morpho-structural features, as follows: Puna, Eastern Cordillera (EC), sub-Andean Ranges (SAR) and Santa Bárbara system (SB) (Fig. 1). The present study deals with the geochemistry of thermal springs located in EC, SAR and SB.

EC is characterized by a series of narrow and elongated blocks limited by two main thrusts, resulting in a double-vergent-fault bounded mountain range (Rodríguez Fernández et al., 1999; Heredia et al., 1999). These blocks show Proterozoic-Cambrian cores (Puncoviscana Formation and Mesón Group; Turner, 1960). Sub-vertical secondary reverse faults with planes dipping west are also common (Moreno Espelta et al., 1978).

SAR is located to the east of the Eastern Cordillera. This morphostructure is characterized by N-NE to S-SW elongated anticlines that develop a series of continuous and parallel brachianticlines with Paleozoic rock cores (Mingramm et al., 1979).

The structural setting of SB system is dominated by inverted faults associated with the Cretaceous-Early Paleocene rift system that developed in NW Argentina (Mingramm et al., 1979; Salfity and Marquillas, 1994; Kley and Monaldi, 2002). This inversion, related to the Andean tectonic cycle, is reflected by the overall westward vergence of anticlines, which have been faulted in their western limbs.

A general stratigraphic column for these three provinces can be summarized as follows:

The basement corresponds to Puncoviscana Formation (Turner, 1960), a low grade metamorphosed sequence comprising green greywackes, interbedded siltstone and mudstone, with local conglomerates and carbonates crossed cut by barite veins. The Middle to Upper Cambrian Mesón Group (Campanario Formation) consists of conglomerate, siltstone, mudstone, and sandstone deposited in a subtidal environment (Sánchez and Salfity, 1999). Early Ordovician sandstones and shales, with subordinate calcareous horizons belonging to the Santa Victoria Group (Turner, 1960) and equivalent units (e.g., Centinela Formation; Harrington, 1957; Monaldi et al., 1986), are overlain by younger, Upper Ordovician to Silurian sandstones and shales of the Zapla Formation (Astini, 2003) both occurring in SAR. Upper Carboniferous-Lower Triassic sedimentary rocks (SAR and SB) include marine and continental sequences covered by marine carbonate sequences (Macharetí and Mandiyutí Formations; Starck et al., 1993). The Neoproterozoic-Lower Triassic sequence is unconformably covered by Cretaceous-Paleocene rocks of the Salta Group (Pirgua, Balbuena and Santa Bárbara Subgroups), deposited during the aforementioned rifting event that took place in NW Argentina. Early to Late Cretaceous Pirgua Subgroup (in SAR and SB) mainly consists of red continental conglomerate and sandstone locally interbedded with, or intruded by alkaline volcanic rocks (Galliski and Viramonte, 1988; Salfity and Marquillas, 1994; Marquillas et al., 2005). Latest Cretaceous to Early Paleocene Balbuena Subgroup (Turner, 1959) consists of continental to marine sandstone, limestone and shales. Within this subgroup, Yacoraite Formation is the main source and reservoir of the petroleum system of the Caimancito oilfield (Disalvo et al., 2002). Santa Bárbara Subgroup (Paleocene to Early Eocene) consists of shales with rare carbonate intercalations characterized by thin clastic facies of lacustrine origin that efficiently seal the underlying formations. Four main formations can be recognized in this Subgroup: Olmedo (halite and gypsum evaporite and dark claystones), Mealla (red claystones), Maíz Gordo (limestones and green claystones) and Lumbrera (red claystones) (Disalvo et al., 2002). The sedimentary column is completed by thick packages of synorogenic continental rocks of the Middle Miocene-Pliocene Orán Group (Russo, 1972; Russo and Serraiotto, 1979). This consists of sandy and pelitic sediments with intercalations of evaporite deposits (Galli and Hernández, 1999). Oolitic limestones, tuff banks and streaks of fibrous gypsum were recognized in restricted horizons (Russo and Serraiotto, 1978; Galli et al., 1996).

3. Materials and methods

3.1. General features of the thermal springs

3.1.1. Eastern Cordillera

Reyes (RE) thermal springs are located at the eastern edge of EC (Fig. 1) and represent one of the main touristic attractions in Jujuy Province. RE emerge from joints of the Campanario Formation (Mesón Group) through a fault that limits the syncline by the west. Thermal waters discharged through an artificial uptake that supplies a cistern with an estimated flow of 200 L/min.

3.1.2. Sub-Andean Ranges

Aguas Calientes (AC) thermal springs emerge along the western edge of the Puesto Viejo hill, likely controlled by fracture systems occurring in the mine of Puesto Viejo. Such a hill is a morphological unit with sub-meridian orientation (Fig. 2.2) in the southern section of Zapla anticline and presents features typical of the Central Sub-Andean range (Baldis et al., 1976a).

El Jordán (EJ) thermal spring is located in El Jordán ravine, within the Calilegua hills that consist of anticlines constituting thrust fronts by sub-meridian faults separated by synclines producing wide valleys (Fig. 1b). In this area, Silurian-Devonian rocks emerge with an approximate maximum thickness of 1000 m (Bianucci, 1973). The sequence also includes Cretaceous calcareous sandstones, oolitic and stromatolitic limestones of the Balbuena Subgroup, as well as siltstones, claystones and marly sandstones of the Santa Bárbara system. The most recent deposits of the Orán Group consist of sandstones and pelites. Thermal springs discharge from joints in reddish sandstones that correspond to the upper level of Devonian sedimentary rocks (Fig. 2.2).

3.1.3. Santa Barbara system

The studied thermal manifestations are associated with the main NNE thrust faults, where local transverse and antithetic faults create structural closures.

Caimancito (CA) thermal springs are at the boundary between the SAR and SB. These waters showed temperatures up 50 °C and a total flow rate of ~1000 L/min (Miranda and Johanis, 2000).

El Palmar (EL) thermal springs are located at the foot of the mountains, where tectonic structures crosscut conditioning their upwelling. They emerge along the Salado stream through fractures in quartzite walls belonging to the Lower Paleozoic Santa Victoria Group. Several travertine deposits were recognized near the springs that showed outlet temperatures ranging from 42 °C to 48 °C with a total flow rate up to 240 L/min (Miranda and Johanis, 2000).

La Quinta (LQ) thermal springs are located at the northern end of the Santa Bárbara hills, on the swampy ground of La Quinta lake whose bottom is covered by a thick layer of peloids. The eastern sector of the lake is adjacent to an old sulfur mine (Santa Bárbara). Along the lake rim, characterized by the presence of green thermophilic algae forming reddish, pink and white-colored deposits, blocks of fine-grained calcareous sandstone, with intercalations of clayed marls (Yacoraite Formation), occur.

Siete Aguas (SA) is a well drilled by YPF (Yacimientos Petroliferos Fiscales) in 1937, down to a depth of 1131 m. Water discharging at 70° to 72 °C is continuously pumped out at ~1 L/min.

3.2. Water and gas sampling

Water samples were collected from 14 thermal discharges: Reyes (RE1, RE2 and RE3), Aguas Calientes (AC1, AC2, and AC3), El Jordan (J), Caimancito (CA1, CA2 and CA3), La Quinta (LQ1, LQ2, and LQ3), El Palmar (EP1, EP2, EP3, EP4, EP5, EP6, and EP7), and Siete Aguas (SA). Outlet water temperature (T), pH and electrical conductivity (EC) were measured in the field with portable instruments (Hanna HI 98195; accuracy: ± 0.15 °C, ± 0.02 and ± 1%, respectively). Waters were sampled in high-density polyethylene (HDPE), as follows: 2 samples filtered at 0.45 μm (Millipore®) and acidified with ultrapure HCl and HNO_3 for the analysis of major cations and trace elements, respectively; 1 filtered sample for the analysis of anions; 1 unfiltered sample for the analysis of water isotopes; 1 unfiltered and diluted (1:10) sample for the analysis of SiO_2; 1 sample in a 50 mL glass flask equipped with a rubber septum, for the analysis of the dissolved gases.

Bubbling gases from LQ1, LQ2, LQ3, AC2, EP2 and SA (Fig. 1) were collected using a plastic funnel up-side-down positioned above the bubbles and connected through tygon tubes to the sampling flasks. The latter consisted of (i) a pre-evacuated 60 mL glass thorion tapped bottle filled with 20 mL of a 4 N NaOH solution for the analysis of the gas chemical composition (Giggenbach and Goguel, 1989) and (ii) a pre-evacuated 60 mL glass flask for the analysis of the organic species and isotopic ratio in CO_2 ($\delta^{13}C$–CO_2) (Vaselli et al., 2006).

3.3. Chemical and isotopic analyses of waters

Total alkalinity was analyzed by acidimetric titration (AT) using HCl 0.01 N. Main anions (F^-, Cl^-, Br^-, NO_3^- and SO_4^{2-}) and cations (Ca^{2+}, Mg^{2+}, Na^+, K^+, NH_4^+ and Li^+) were analyzed at the Laboratory of Fluid Geochemistry of the University of Florence (Italy) by ion-chromatography (IC) using Metrohm 761 and Metrohm 861 chromatographs, respectively. The analytical errors for AT and IC were ≤5%. The SiO_2 concentrations were determined by spectrophotometry (SP) after the addition of a 10% (w/v) ammonia molybdate solution in a sulfuric acid environment (Bencini and Martini, 1979), while B was analyzed by molecular absorption spectrometry (MAS; Philips UNICAM) using the Azomethine-H (AH) method (Bencini, 1985). The analytical error for SP and MAS was ≤5%. Selected trace elements (Mn, Fe, Ba, As, and Sb) were analyzed at the University of Florence by Inductively Coupled Plasma Optical Emission Spectrometry (ICP-OES) using an Optima 8000 PerkinElmer spectrometer. The analytical error for ICP-OES was ≤10%. The $^{18}O/^{16}O$ and $^{2}H/^{1}H$ ratios of water (expressed as $\delta^{18}O–H_2O$ and $\delta D\text{-}H_2O$ ‰ vs. V-SMOW) were determined at the Laboratory of Stable Isotopes of Parma (Italy) by isotope ratio mass spectrometry (IRMS). Oxygen isotopes measurements were carried out by using a Gas Bench peripheral coupled with a Thermo Delta V mass spectrometer. A TC-EA peripheral interfaced by means of a ConFloIV with Thermo Delta XP mass spectrometer was used for hydrogen isotopes. The analytical errors for IRMS were ± 0.1‰ for δ18O and better than ± 1‰ for δD.

3.4. Chemical and isotopic analysis of dissolved and bubbling gases

The analysis of N_2, (Ar + O_2), H_2 and He in the headspace of the soda flasks, as well as those of CO_2, N_2, (Ar + O_2), and He in the headspace of the flasks used to sample the dissolved gases, was carried out at the University of Florence (Italy) by gas chromatography (GC) using a Shimadzu 15 A instrument equipped with a Thermal Conductivity Detector (TCD). Argon and O_2 were analyzed using a Thermo Focus gas chromatograph equipped with a 30 m long capillary molecular sieve column and a TCD. Methane (in both dissolved and bubbling gases) and light hydrocarbons (in bubbling gases) were determined by using a Shimadzu 14 A gas chromatograph equipped with a Flame Ionization Detector (FID) and a 10 m long stainless steel column packed with Chromosorb PAW 80/100 mesh coated with 23% SP 1700 (Vaselli et al., 2006). The analytical error for the GC analysis was ≤10%. Carbon dioxide (as CO_3^{2-}) and H_2S (as SO_4^{2-} after oxidation with H_2O_2) in the soda solution were measured by AT (using HCl 0.1 N) and IC, respectively. The concentrations (in mmol/mol) of the dissolved gases were given by the sum of $n_{i,g}$ and $n_{i,l}$, which are the moles of the gas compound *i* in the gas and the liquid portion of the sampling flasks respectively. The $n_{i,g}$ values were computed on the basis of the GC analysis of the gases stored in the sampling flask headspace, whereas the $n_{i,l}$ values were calculated from the $n_{i,g}$ ones by means of the Henry's law constants (Wilhelm et al., 1977), assuming that in the sampling flasks the separated gas phase was in equilibrium with the liquid. The partial pressures of each gas species (in mbar) were then computed, based on the total mole values according to the ideal gas law.

The $\delta^{13}C–CO_2$ values of both bubbling and dissolved gases were determined at the Laboratory of Stable Isotopes of CNR-IGG (Consiglio Nazionale delle Ricerche, Istituto Geotermia e Georisorse) in Pisa (Italy) by using a Finnigan Delta S mass spectrometer (MS), after extracting and purifying CO_2 by using liquid N_2 and N_2- trichloroethylene cryogenic traps (Evans et al., 1998; Vaselli et al., 2006). Internal (Carrara and S. Vincenzo marbles) and international (NB18 and NBS19) standards were used for estimating the external precision. Analytical uncertainty and the reproducibility were ± 0.05‰ and ± 0.1‰, respectively. Carbon dioxide released from the water to the headspace of the dissolved gas sampling flasks was affected by isotope fractionation. The measured $\delta^{13}C–CO_2$ values of these gas aliquots ($\delta^{13}C–CO_{2STRIP}$) were used to compute the $\delta^{13}C$ values of dissolved CO_2 according to the ε1 fractionation factor for the gas–water equilibrium (Zhang et al., 1995), as follows:

$$\epsilon_1 = \delta^{13}C–CO_2 - \delta^{13}C–CO_{2STRIP} = (0.0049 \times T) - 1.31 \quad (1)$$

The $\delta^{13}C$ values of CH_4 ($\delta^{13}C–CH_4$) from bubbling gases were analyzed by mass spectrometry (Varian MAT 250), according to the procedure reported by Schoell (1980). The analytical uncertainly was ± 0.15‰. In the dissolved gases, CH_4 concentration in the dissolved gases was too low to allow any analysis of $\delta^{13}C–CH_4$.

The $^3He/^4He$ (expressed as R/Ra, where R is the $^3He/^4He$ measured in the sample and Ra is the $^3He/^4He$ ratio in the air: $1.39\ 10^{-6}$; Mamyrin and Tolstikhin, 1984) and $^4He/^{20}Ne$ ratios were determined at the Laboratory of Noble gas isotopes of INGV (Istituto Nazionale di Geofisica e Vulcanologia) in Palermo (Italy). Helium and neon were purified from the gas mixture in an ultra-high-vacuum line and then separately introduced into two distinct mass spectrometers: a split-flight-tube (GVI Helix SFT) for helium isotopes and a multicollector (Thermo Helix MC plus) for neon isotopes. The analytical error on $^3He/^4He$ was ≤1%, while on ^{20}Ne was < 0.1%. Further details on the analytical protocol adopted at INGV laboratory can be found in Rizzo et al. (2015, 2016, 2019). The measured R/Ra values were corrected for air contamination using the $^4He/^{20}Ne$ ratios (Poreda and Craig, 1989), as follows:

$$Rc/Ra = [(R/Ra) – r)]/(1\text{-}r) \quad (2)$$

where $r = (^4He/^{20}Ne)_{air}/(^4He/^{20}Ne)_{meas}$, the $(^4He/^{20}Ne)_{air}$ ratio being that in the atmosphere (0.318; Ozima and Podosek, 1983) and the $(^4He/^{20}Ne)_{meas}$ ratio that measured in the gas sample.

4. Results

4.1. Chemical and isotopic ($\delta^{18}O–H_2O$, $\delta D\text{-}H_2O$) composition of waters

Geographic coordinates, outlet temperatures, pH and Total dissolved Solids (TDS) values, as well as the chemical composition (in mg/L) and the $\delta^{18}O–H_2O$ and $\delta D\text{-}H_2O$ values of the thermal springs from the study area, are reported in Table 1. Water temperatures ranged from 22.1 °C (AC3) to 72 °C (SA). The pH values varied from slightly acidic (5.5; EP7) to slightly alkaline (8.21; CA3). Low TDS (≤135 mg/L) waters from Reyes (RE2 and RE3) in *EC* area had a Ca^{2+}-HCO_3^- composition, whereas RE1, characterized by relatively high TDS (1054 mg/L) and high temperature (47.9 °C), showed a Na^+-SO_4^{2-} composition (Fig. 2a–c). AC waters from *SAR* showed relatively low TDS values (≤527 mg/L) and a $Ca^{2+}(Mg^{2+})$-HCO_3^- composition, whereas EJ had a high TDS (2995 mg/L and Na^+-Cl^--(SO_4^{2-}) composition (Fig. 2a–c). CA and EP waters from *SB* showed relatively high TDS (from 1392 to 4432 mg/L) and temperatures (from 41.7 to 49.3 °C) and a Na^+-SO_4^{2-} composition. Differently, SA had a Na^+-HCO_3^- composition (Fig. 2a–c), relatively low TDS (992 mg/L) and the highest temperature of the dataset (72 °C). Waters from LQ, in *SB*, showed outlet temperatures ranging from 46.1 to 55 °C, the highest TDS values (up to 16,256 mg/L) and a Na^+-Cl^- composition (Fig. 2a–c).

The concentrations of Li^+, NH_4^+ and B in RE and AC waters were up to 0.11, 0.11 and 0.51 mg/L, respectively, whereas those of the other thermal waters increased, consistently with the TDS values, up to 15, 8 and 7.8 mg/L, respectively (LQ waters), except SA water for which relatively high NH_4^+ concentrations (4.9 mg/L) were measured notwithstanding its low TDS value (Table 1). Silica concentrations followed a distribution similar to those of the minor compounds, ranging from 41 to 52 mg/L at RE, AC and SA, and from 46 to 168 at EJ, CA, EP, and LQ. The NO_3^- concentrations in LQ waters were up to 12–13 mg/L, whereas they were in a wide range (from 0.03 to 7.3 mg/L) in the remaining thermal waters, with no clear distinction among them. The concentrations of Mn and Fe (Table 1) in EP and LQ waters were up to

Table 1
Geographic coordinates, outlet temperatures, TDS and pH values, chemical and isotopic ($\delta^{18}O$–H_2O and δD-H_2O, in ‰ vs. V-SMOW) composition of thermal waters from Jujuy Province. Concentrations are expressed in mg/L.

	Coordinates		type	zone	altitude	T °C	pH	HCO_3^-	F	Cl	Br	NO_3^-	SO_4^{2-}	Ca^{2+}	Mg^{2+}	Na^+	K^+	NH_4^+	Li^+	SiO2	B	TDS	δ18O–H2O	δD-H2O
RE1	S 24° 10′ 20″	W 65° 29′ 28″	TS	EC	1766	47.9	7.69	207	0.66	19	0.011	3.2	476	65	8.2	211	11	0.07	0.21	52	0.31	1054	−9.8	−71
RE2	S 24° 10′ 21″	W 65° 29′ 18″	TS	EC	1794	22.3	8.32	46	0.40	3.0	0.005	7.3	10	8.0	4.8	5.8	2.8	0.08	0.18	42	0.25	131	−9.3	−67
RE3	S 24° 10′ 22″	W 65° 29′ 18″	TS	EC	1794	21.3	8.35	44	0.25	5.3	0.007	6.0	14	9.0	5.0	5.4	2.4	0.05	0.08	43	0.12	135	−9.2	−67
AC1	S 24° 33′ 4″	W 64° 56′ 38″	TS	SAR	650	28.5	7.54	208	0.31	10	0.009	2.2	35	47	7.6	31	4.3	0.06	0.15	51	0.41	397	−9.6	−69
AC2	S 24° 35′ 30″	W 64° 54′ 35″	TS	SAR	598	29.0	7.74	177	0.22	3.6	0.006	2.2	22	33	4.6	32	3.1	0.06	0.09	48	0.35	326	−9.7	−70
AC3	S 24° 33′ 20″	W 64° 58′ 21″	river	SAR	635	22.1	6.95	332	0.68	8.5	0.008	0.13	30	65	17	27	4.7	0.11	0.11	41	0.51	527	−12.5	−93
EJ	S 23°39′52′	W 66°27′58″	TS	SAR	786	28.7	7.11	467	1.3	750	0.44	3.4	701	104	34	860	21	3.5	1.62	46	0.88	2995	−6.2	−42
CA1	S 23° 44′39″	W 64°31′11″	TS	SB	310	49.3	7.88	177	2.9	221	0.15	0.74	459	21	0.64	389	3.7	4.0	0.17	112	0.85	1392	−9.7	−70
CA2	S 23° 44′40″	W 64°31′11″	TS	SB	310	43.3	8.14	187	2.9	225	0.20	1.0	476	22	0.84	414	3.3	2.3	0.27	107	0.77	1443	−9.5	−69
CA3	S 23° 44′2″	W 64°31′10″	TS	SB	393	49.0	8.21	213	3.7	235	0.24	1.1	532	21	0.72	480	2.3	4.3	0.25	115	0.93	1610	−9.2	−66
EP1	S 24°4′51″	W 65°32′7″	TS	SB	842	41.7	6.71	1110	2.7	502	0.99	2.6	1060	163	38	910	62	4.8	3.5	136	1.6	3999	−7.5	−51
EP2	S 24°4′52″	W 65°32′6″	TS	SB	844	47.9	6.66	1230	2.6	594	1.2	1.9	1110	191	43	1050	62	5.4	3.8	131	1.7	4432	−7.2	−48
EP3	S 24° 4′51″	W 65° 32′ 8″	TS	SB	846	42.1	6.59	1100	2.4	465	0.99	2.2	988	158	36	887	54	3.8	3.3	135	1.5	3841	−7.6	−55
EP4	S 24° 4′50″	W 64°32′5″	TS	SB	928	48.4	5.74	1135	3.2	615	1.4	2.6	1132	164	38	981	63	3.5	3.5	132	2.1	4276	−7.3	−50
EP5	S 24° 4′51″	W 64°32′6″	TS	SB	929	42.2	5.63	1031	3.3	501	1.2	3	1021	172	36	838	57	3.3	3.5	14	1.9	3686	−7.5	−48
EP6	S 24° 4′51″	W 64°32′5″	TS	SB	927	42.9	5.52	1010	4.1	496	1.2	2.5	1025	170	37	818	58	4.1	3.4	135	1.8	3766	−7.7	−52
EP7	S 24° 4′51″	W 64°32′6″	TS	SB	925	41.4	5.50	1016	5.5	481	1.2	1.1	980	145	34	823	57	2.9	3.3	126	2.2	3678	−7.4	−54
SA	S 23°51′44″	W 64°25′49″	well	SB	556	72.0	7.49	316	1.3	137	0.10	0.03	210	62	18	171	20	4.9	0.31	51	0.31	992	−9.9	−73
LQ1	S 23° 53′ 7″	W 64° 27′ 58″	TS	SB	620	54.05	6.02	857	4.8	7891	6.6	12	1345	728	134	4644	350	6.8	15	161	6.9	16,162	−7.8	−71
LQ2	S 23° 53′ 6″	W 64° 28′ 00″	TS	SB	632	55.0	6.01	940	7.5	8234	2.5	13	1175	402	89	4853	347	8.0	11	166	7.5	16,256	−8.0	−73
LQ3	S 23° 53′ 6″	W 64° 27′ 59″	TS	SB	625	46.08	6.49	775	4.4	8246	2.6	12	1120	394	84	4828	345	7.1	9.3	168	7.8	16,003	−8.1	−70

51 and 1233 μg/L, i.e. 1-3 orders of magnitude higher than those measured in the other thermal springs. LQ and EP waters, as well as those from *SB* area (CA and SA), were also enriched in Sb (up to 1562 μg/L). The As concentrations in LQ, EP and RE1 waters (up to 207 μg/L) were 1–2 orders of magnitude higher than in the other waters. The highest Ba concentrations (up to 368 μg/L) were measured in AC, SA, RE2, and RE3 waters, while LQ, EP, CA, and RE1 waters showed significantly lower concentrations (≤58 μg/L).

The $\delta^{18}O$–H_2O and δD-H_2O values (Table 1) in all thermal waters ranged from −7.2‰ to −12.5‰ vs. V-SMOW and −42‰ a −73‰ vs. V-SMOW, respectively.

4.2. Chemical and isotopic composition of dissolved and free gases

The chemical composition (in mmol/mol) of gases dissolved in thermal waters are shown in Table 3, where the $\delta^{13}C$–CO_2 and $\delta^{13}C$–CH_4 values (in ‰ vs. V-PDB), as well as the Rc/Ra values and the $^4He/^{20}Ne$ ratios, are reported. Carbon dioxide was the main component of samples from RE, AC, EP and SA (from 542 to 804 mmol/mol), followed by significant concentrations (from 188 to 426 mmol/mol) of N_2, the latter being the main component for EJ and CA gases (from 535 to 718 mmol/mol). Argon concentrations ranged from 4.5 to 18 mmol/mol, whereas those of O_2 were in a wider range from 3 to 92 mmol/mol. Methane concentrations were low (≤0.094 mmol/mol) except for SA (0.42 mmol/mol). Neon and He concentrations ranged from 0.0030 to 0.0086 and from 0.0041 to 0.026 mmol/mol, respectively. The $\delta^{13}C$–CO_2 values of RE, AC, EP and SA gases were higher (from −13.6‰ to −11.5‰ vs. V-PDB) than those from EJ and CA (up to −18.7‰ vs. V-PDB).

Bubbling gases from LQ, EP and SA (in mmol/mol; Table 3) mostly consisted of CO_2 (from 924 to 950 mmol/mol) with minor concentrations of N_2 (from 45 to 74 mmol/mol), Ar (from 1.1 to 1.6 mmol/mol), O_2 (from 1 to 3.4 mmol/mol), and CH_4 (from 0.089 to 0.89 mmol/mol). Significant H_2 concentrations (from 0.0052 to 0.0077 mmol/mol) were also measured. The $\delta^{13}C$–CO_2 values, consistently with those of the dissolved gases, were ranging from −10‰ and −12.1‰ vs. V-PDB (Table 3). The $\delta^{13}C$–CH_4 values were in a large range, from −60.2‰ (AC) to −33.7‰ vs. V-PDB (LQ3). The $^3He/^4He$ values ranged from 0.09 to 0.21 Ra with limited atmospheric contamination, as indicated by the $^4He/^{20}Ne$ ratios ranging from 4.5 to 5.9.

5. Discussion

5.1. Processes controlling the chemistry of waters

The origin of thermal waters was investigated on the basis of the $\delta^{18}O$–H_2O and δD-H_2O values plotted in a binary diagram (Fig. 3), where the Local Meteoric Water Line ($\delta D = 8.29 \times \delta^{18}O + 11.75‰$; Hoke et al., 2013) and the gradient of $\delta^{18}O$–H_2O fractionation with altitude (−2.62‰/km) calculated on the basis of rainwater data (Peralta Arnold et al., 2017), were reported. Most waters plot along the LMWL, indicating a meteoric origin and recharge altitudes at 2500–3000 m a.s.l. for RE, AC, CA, and SA, from 1800 to 2100 m a.s.l. for EP and ~1500 m a.s.l. for EJ. LQ waters, having a calculated recharge area at 2800–3000 m a.s.l., showed a significant ^{18}O enrichment, likely caused by water-rock interaction at relatively high temperatures (> 150 °C; Truesdell and Hulston, 1980). This is consistent with the high TDS values and the Na^+-Cl^- composition of these waters (Table 1 and Fig. 2a–c), which are typical features of a geothermal brine. Binary plots comparing the molar concentrations of the main cation-anion pairs were used to investigate the interaction of thermal waters with different rocks. As shown in the $(Ca^{2+} + Mg^{2+})$ vs. HCO_3^- diagram (Fig. 4a), waters having a Ca^{2+}-HCO_3^- composition (RE2, RE3 and those from AC) approached the stoichiometric ratio. This indicates that their chemistry was mainly related to a shallow underground circulation pattern within the Quaternary deposits, as supported by their

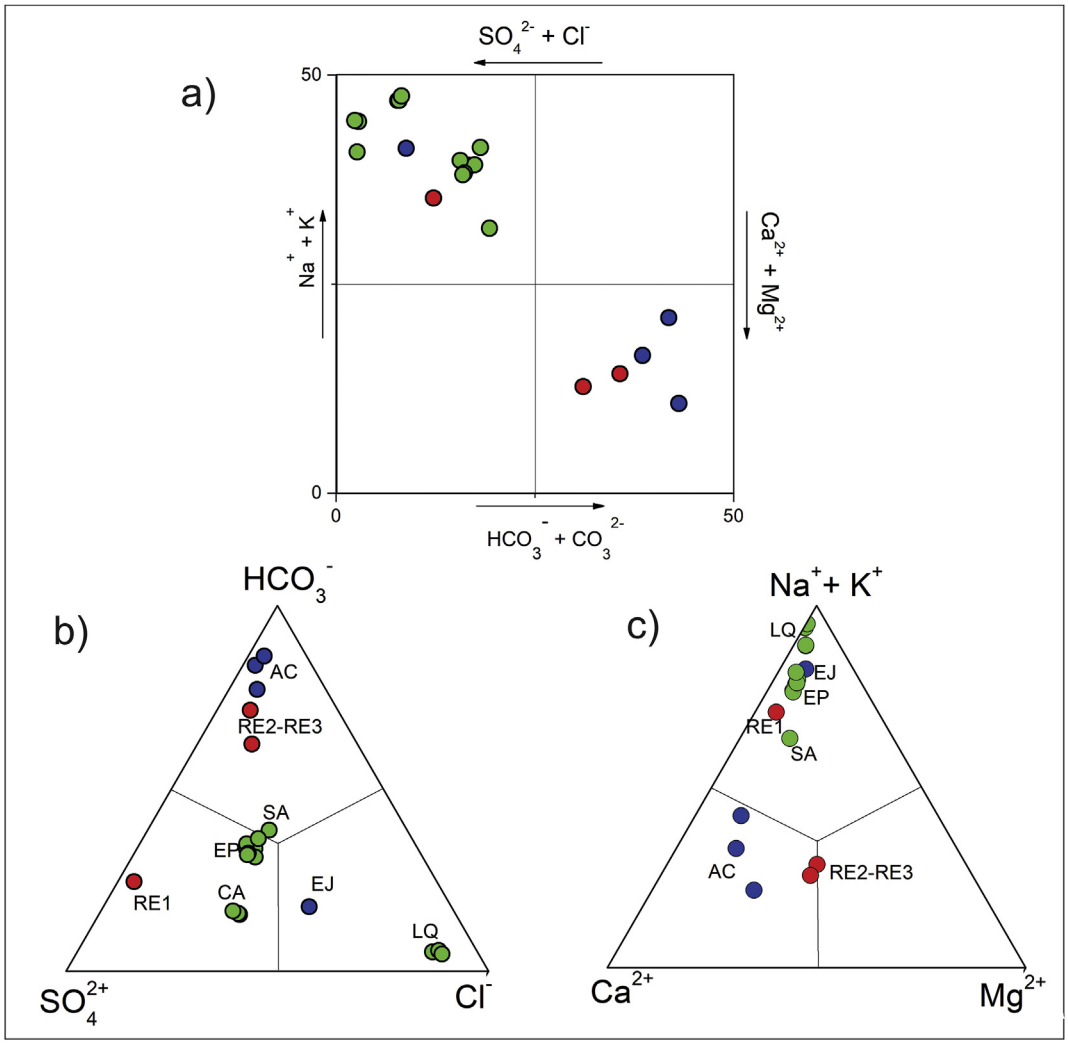

Fig. 2. (a) Langelier-Ludwig diagram (Langelier and Ludwig, 1942), (b) SO_4^{2-}-Cl^--HCO_3^- and (c) Ca^{2+}-($Na^+ + K^+$)-Mg^{2+} ternary diagrams for thermal waters from Jujuy Province. Symbols as in Fig. 1.

relatively low outlet temperatures and TDS values (Table 1). RE1 water from *EC*, although plotting on the stoichiometric ($Ca^{2+} + Mg^{2+}$)/HCO_3^- line (Fig. 4a), cannot be related to such a shallow circulation system and would be the most representative of the reservoir of RE, due to its relatively high temperature and TDS values and the Na^+-SO_4^{2-} composition (Fig. 2a–c). Interaction with S-bearing rocks, such as gypsum from deposits of the Anta Formation ascribed to Orán Group, followed by Ca^{2+}-Na^+ exchange with clay minerals, likely led to this uncommon chemical composition. Similar chemical features were also shown by CA and EP waters from *SB* (Fig. 2a–c), where evaporite deposits of Salta Group occur. Depletion of Ca^{2+} due to Ca^{2+}-Na^+ exchange between thermal waters and clays may explain the low ($Ca^{2+} + Mg^{2+}$)/SO_4^{2-} mol-ratios shown by these waters (Fig. 4b). However, the relatively high Cl^- shown concentrations (Fig. 4c) suggest a contribution from the dissolution of evaporite, including halite, the latter being recognized in Olmedo (Salta Group) and Anta (Orán Group) formations. The chemistry of EJ water, whose compositional features were similar to those from CA and EP (Table 1), was likely depending on the same processes, since slight differences in the Cl^-/SO_4^{2-} ratios were likely produced by the heterogeneous distribution of S- and Cl-bearing minerals in the evaporitic horizons in contact with the circulating waters. Hence, LQ waters, showing a marked Cl^- (and Na^+) enrichment, were probably in contact with evaporite sequences dominated by halite facies over sulphate facies (Fig. 4d). The Na^+-HCO_3^- composition of the SA water from *SB*, coupled with its relatively low salinity, implies a limited interaction with evaporite deposits. This is apparently in contrast with the high outlet temperature of SA. However, it has to be considered that this water sample was pumped out from a great depth (> 1000 m), thus preventing, at least partially, water cooling that, on the contrary, can affect naturally discharging thermal springs. Halite dissolution may yield Cl^-/Br^- ratios > 1000 (e.g. Alcalá and Custodio, 2008; McCaffrey et al., 1987), such as those of most thermal waters (CA, LQ, RE1 and, at a lesser extent, SA; Fig. 5a), whereas lower ratios must be ascribed to dominant groundwater (RE2, RE3 and AC waters). The low Cl^-/Br^- ratios characterizing EP waters (Fig. 5a) may be due to different causes, including interaction with limestone and/or contribution of seawater trapped in the marine sediments (Cartwright et al., 2006, and references therein). However, the latter hypothesis is likely to be discarded since a significant seawater addition would imply D- and ^{18}O-enrichments with respect to the recharging meteoric water, in contradiction with the distribution of samples in Fig. 3. The relatively high B concentrations measured in the CA, EJ, EP and LQ waters (Fig. 5b) can be interpreted as due to interaction with (i) evaporite deposits and/or (ii) basement rocks. An involvement of the basement is consistent with the occurrence of a reduction of the crustal thickness and deep detachment affecting the basement in SB system, as suggested by Kley and Monaldi (2002) and Whitman et al. (1996). Mature (or partially mature) hydrothermal waters are also typically rich in Li^+, this element being released during water-rock interactions and intimately dependent on the temperature

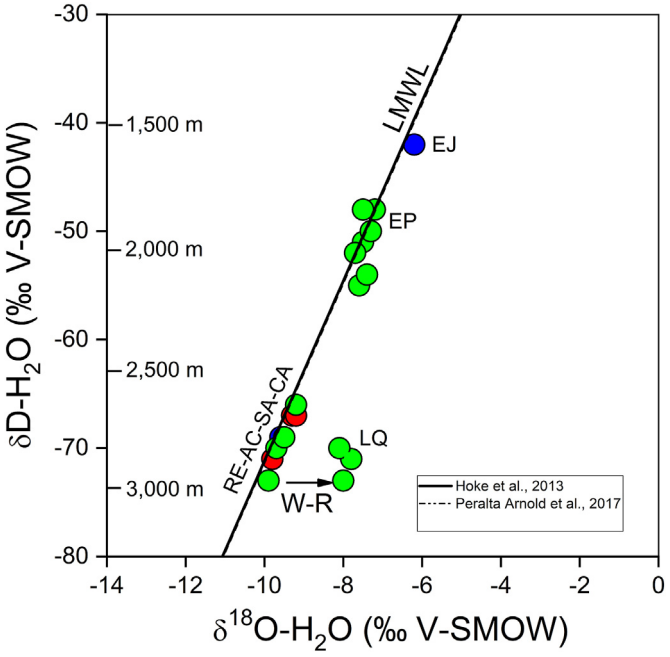

Fig. 3. δD-H_2O vs. $\delta^{18}O$–H_2O (as ‰ vs. V-SMOW) binary diagram for thermal waters from Jujuy Province. The Local Meteoric Water Line (LMWL: δD-H_2O = 8.29 × $\delta^{18}O$–H_2O + 11.75; Hoke et al., 2013 and δD-H_2O = 8.3 × $\delta^{18}O$–H_2O + 11.67) and the gradient of $\delta^{18}O$–H_2O fractionation with altitude calculated on the basis of rainwater data (Peralta Arnold et al., 2017) are reported. Symbols as in Fig. 1.

(e.g. Fouillac and Michard, 1981; Arehart et al., 2003). Accordingly, Li^+ and B concentrations followed a similar distribution (Fig. 5b and c). The strong affinity of NH_4^+ for the gaseous phase makes this compound an efficient geochemical tracer for geothermal prospections (e.g., Tonani, 1970; Martini et al., 1984). The relatively high NH_4^+ concentrations shown by the medium-to-high TDS thermal waters (Fig. 5d) are thus a clear indication for hot vapor addition. Boron, NH_4^+ and Li^+ concentrations were related to those of Fe, Mn, As and Sb (Table 2), as these elements are commonly enriched in hydrothermal fluids (Aiuppa et al., 2006; Kaasalainen and Stefánsson, 2012; Wilson et al., 2012; Göb et al., 2013). Barium concentrations in low-TDS thermal waters were higher than those in EP, RE1 and LQ waters, likely due to calcite precipitation, since this element is commonly incorporated in carbonate minerals. Accordingly, saturation indexes (SI), calculated using the PHREEQC Version 3.1.4 software (Parkhurst and Appelo, 1999), indicate that EJ, EP and LQ waters were oversaturated in calcite, aragonite, and dolomite, whereas all waters were undersaturated in gypsum, anhydride and halite (Table 4).

5.2. Origin of gases

The chemical features of bubbling and dissolved gases were basically produced by mixing between an extra-atmospheric component, rich in CO_2 and, secondarily, CH_4, with air contributing, at various degrees, for N_2, Ar and O_2. In fact, all gas samples had N_2/Ar ratios consistent with air saturated water (ASW; Fig. 6). Hydrogen, which was detected in bubbling gases although at relatively low concentrations, was likely produced within the hydrothermal environment, being this gas favored by reducing conditions and temperature. Similarly, the $\delta^{13}C$–CH_4 values (Table 3) suggest that CH_4 originated by thermogenic

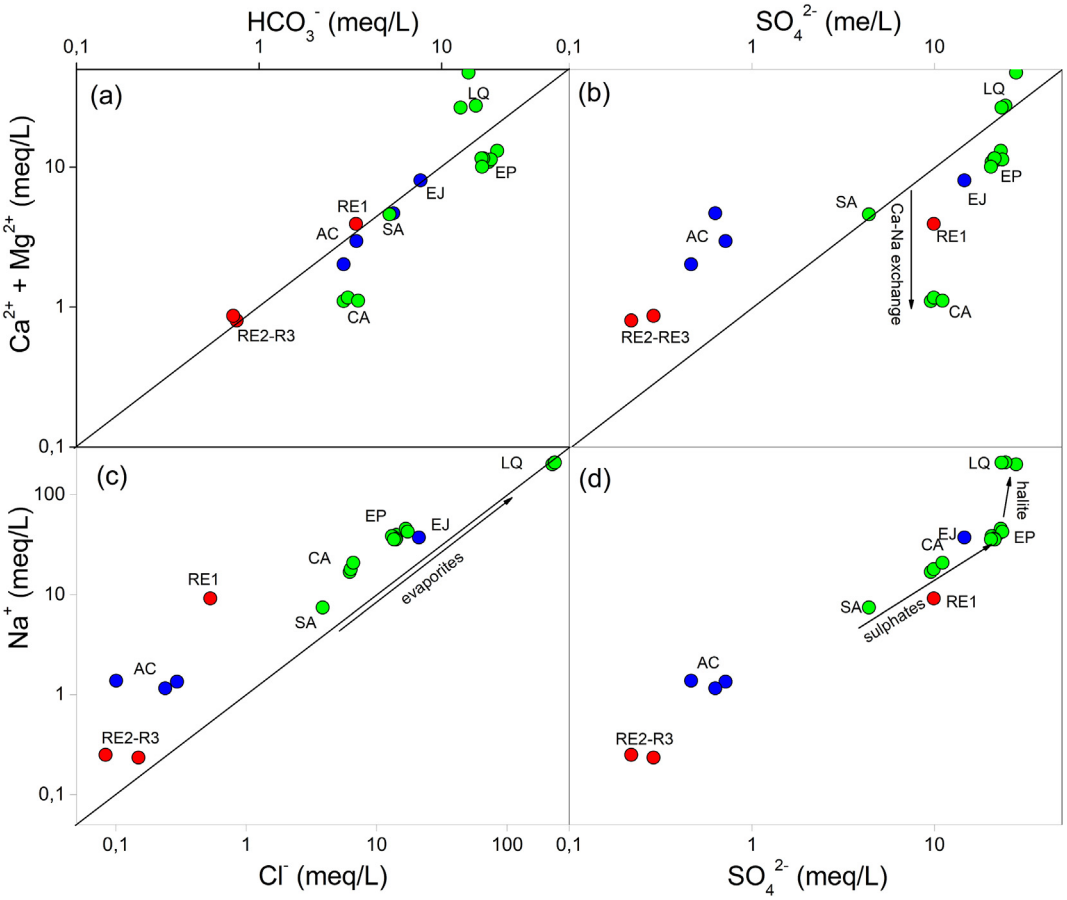

Fig. 4. (a) (Ca^{2+} Mg^{2+}) vs. HCO_3^-, (b) (Ca^{2+} Mg^{2+}) vs. SO_4^{2-}, (c) Na^+ vs. Cl^- and (d) Na^+ vs. SO_4^{2-} binary diagrams for waters from Jujuy province. Concentrations are in meq/L. Symbols as in Fig. 1.

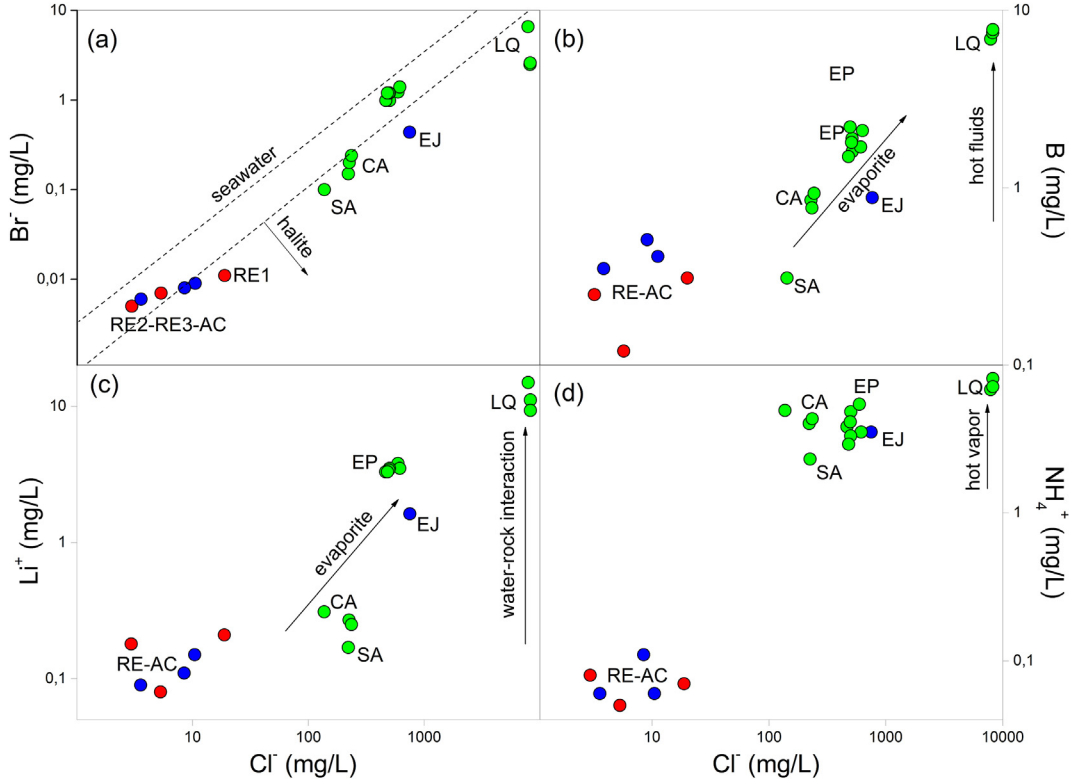

Fig. 5. (a) Br^- vs. Cl^-, (b) B vs. Cl^-, (c) Li^+ vs. Cl^- and (d) Nh_4^+ vs. Cl^- binary diagrams for waters from Jujuy province. Concentrations are in mg/L. Symbols as in Fig. 1.

Table 2
Concentrations (in μg/l) of minor elements (Mn, Fe, Co, Ni, Cu, Zn, Ba, As, and Sb) in of thermal waters from Jujuy Province.

	Mn	Fe	Ba	As	Sb
RE1	3.2	12	30	207	5.4
RE2	2.7	4.7	366	10	4.4
RE3	2.6	19	368	14	3.9
AC1	2.4	5.6	118	13	3.8
AC2	2.9	5.5	175	9.6	2.3
AC3	3.8	5.8	240	7.9	1.9
EJ	8.3	3.4	33	9.3	53
CA1	7.7	61	58	5.6	920
CA2	8.3	7.5	43	4.9	1105
CA3	7.6	33	48	3.5	1175
EP1	445	1021	32	141	1066
EP2	434	646	36	104	719
EP3	550	1171	36	134	1172
EP4	541	895	41	145	1203
EP5	517	716	35	121	985
EP6	475	814	39	118	956
EP7	444	823	33	120	888
SA	63	46	171	2.8	808
LQ1	713	941	45	188	1562
LQ2	751	1233	39	156	1487
LQ3	733	1178	41	195	1502

processes, i.e. degradation of pre-existing organic matter at hydrothermal conditions, except those of RE gases whose isotopic composition implies a biogenic source (e.g. Schoell, 1980, 1988). The $\delta^{13}C$–CO_2 values highlight the occurrence of (i) a shallow CO_2 source related to degradation of organic matter, which is characterized by a strongly negative isotopic signature (−20‰ vs. V-PDB; Degens, 1969; Rollinson, 1993; Sano and Marty, 1995), and (ii) a deeper hydrothermal-type contribution richer in ^{13}C likely related to interaction with limestone (Rollinson, 1993; Ohmoto and Goldhaber, 1997; Hoefs, 2009). The contribution of biogenic CO_2 seems to dominate EJ and CA

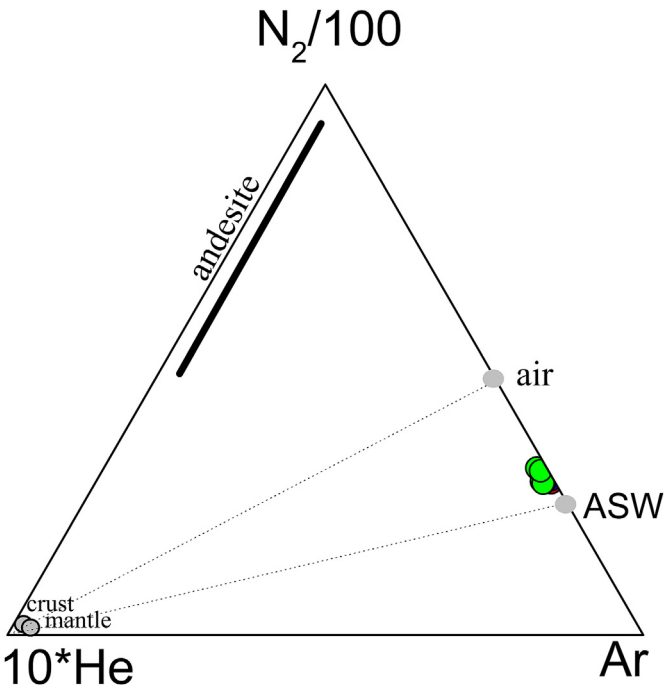

Fig. 6. 10*He vs. N_2/100 vs. Ar ternary diagram for bubbling gases from Jujuy province. Air, crust, mantle and atmospheric saturated waters (ASW) are reported. Symbols as in Fig. 1.

gases, whereas EP, RE, AC, SA and LQ gases were mainly related to the hydrothermal component. The Rc/Ra values (Table 3) indicate that emitted fluids are mostly of crustal origin (0.01–0.05 Ra, Poreda and Craig, 1989; Hilton et al., 2002), although the presence of a mantle He in LQ gases up to 2.6% cannot be completely discarded. The mantle

Table 3
Chemical and isotopic composition ($\delta^{13}C–CO_2$, in ‰ vs. V-PDB) of gases dissolved in thermal waters and bubbling gases from Jujuy Province. $^4He/^{20}Ne$ ratios, $\delta^{13}C–CH_4$ (in ‰ vs. V-PDB) and Rc/Ra values measured in bubbling gases were reported. Concentrations are expressed in mmol/mol.

	co$_2$	N$_2$	^{CH}a	Ar	2	^{H}2	Ne	He	s^{13}c − co$_2$	Rc/Ra	'HePNe	ö^{13}c − ch$_4$	%LIM	%SED	%MORB
RE1	720	269	0.080	6.9	4.3		0.0040	0.0086	−12.5						
RE2	627	355	0.089	8.9	8.9		0.0047	0.0041	−12.9			−59.3			
RE3	669	317	0.094	8.2	6.5		0.0041	0.0076	−13.1			−60.2			
AC1	542	426	0.026	10	22		0.0054	0.0054	−13.6						
EJ	172	718	0.011	18	92		0.0086	0.011	−18.7						
CA1	393	571	0.051	14	22		0.0075	0.024	−16.4						
CA2	363	592	0.063	15	30		0.0073	0.022	−17.6			−41.7			
CA3	426	535	0.035	12	26		0.0062	0.026	−17.1						
EP1	656	323	0.012	7.4	14		0.0046	0.013	−13.1						
EP3	704	280	0.014	6.3	9.9		0.0036	0.014	−13.6						
SA	804	188	0.42	4.5	3.0		0.0030	0.0060	−11.5			−39.2			
EP2	950	45	0.095	1.1	3.4	0.0061	0.0006	0.0033	−11.9	0.09	5.9	−44.9	60	40	0.05
SA	934	61	0.89	1.6	2.1	0.0052	0.0009	0.0039	−10.0	0.11	4.6	−36.6	67	33	0.08
LQ1	935	63	0.12	1.6	1.0	0.0063	0.0009	0.0045	−10.1	0.21	4.5	−34.5	66	33	0.20
LQ2	929	69	0.11	1.6	1.1	0.0077	0.0009	0.0036	−11.0	0.17	5.1	−36.4	63	37	0.12
LQ3	924	74	0.089	1.7	1.2	0.0059	0.0009	0.0031	−10.4	0.15	3.9	−33.7	65	35	0.09

contribution is calculated with the following relation:

$$Mc = \frac{\left(\frac{Rc}{Ra}\right)sample}{\left(\frac{Rc}{Ra}\right)mantle} \cdot 100 \quad (3)$$

where Mc is the mantle contribution, (Rc/Ra)sample is the $^3He/^4He$ measured in each gas sample, and (Rc/Ra)mantle is the hypothetical $^3He/^4He$ ratio of the local mantle assumed as MORB-like (8 ± 1 Ra, Graham, 2002) (Batista Cruz et al., 2019). However, this mantle proportion is significantly lower than in gases from the Puna region (15–20%; Peralta Arnold et al., 2017).

Further insights into the origin of the main gas constituent, i.e. CO_2, can be obtained by inspecting the $CO_2/^3He$ vs. $\delta^{13}C–CO_2$ diagram (Sano and Marty, 1995). As shown in Fig. 7, EP, SA and LQ gases plot far from the mantle field, at an intermediate position between the limestone and organic matters fields. The CO_2 contributions from MORB (M), limestone (L) and organic-rich sediments (S) can be quantified, as follows (Sano and Marty, 1995):

$$(\delta^{13}C–CO_2)_{meas} = M(\delta^{13}C–CO_2)_{MORB} + L(\delta^{13}C–CO_2)_{Lim} + S(\delta^{13}C–CO_2)_{Sed} \quad (4)$$

$$1/(CO_2/^3He)_{meas} = M/(CO_2/^3He)_{MORB} + L/(CO_2/^3He)_{Lim} + S/(CO_2/^3He)_{Sed} \quad (5)$$

$$M + L + S = 1 \quad (6)$$

Subscripts *meas*, *MORB*, *Lim*, and *Sed* refer to the sample, MORB (a proxy to the upper mantle), limestone and organic sediment, respectively, whereas for computations the end members have the following

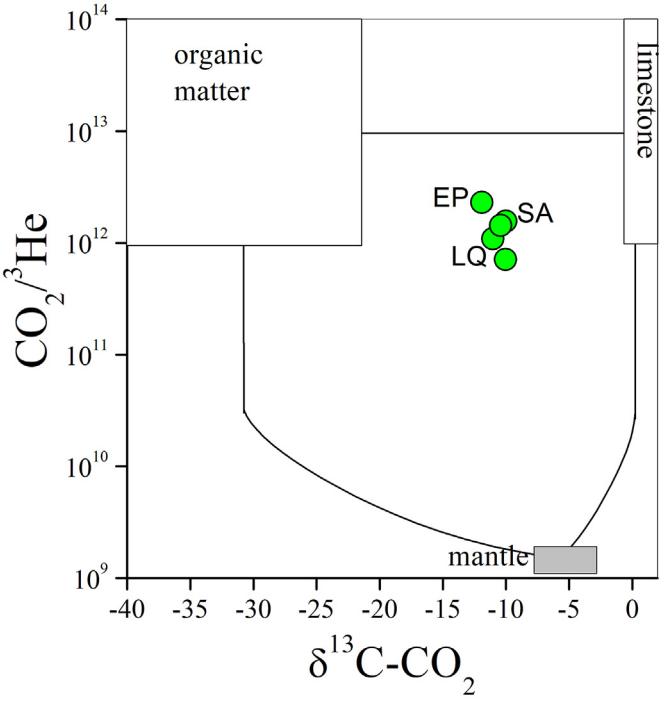

Fig. 7. $CO_2/^3He$ vs. $d^{13}C–CO_2$ binary diagram for bubbling gases from Jujuy province where the composition of gases from limestone, MORB and organic sediment are reported (Sano and Marty, 1995). Symbols as in Fig. 1.

Table 4
Saturation indexes (SI) of the mineral species that had values near to equilibrium or that were oversaturated.

id	Anhydrite	Aragonite	Barite	Ca leite	Chalcedony	Dolomite	Gypsum	Halite	Magnesite	Quartz
RE3	−1.1	−0.7	0.2	−0.5	0.3	−0.6	−1.1	−7.0	−1.5	0.6
AC1	−2.3	−0.5	0.1	−0.4	0.6	−0.2	−2.2	−8.0	−1.4	0.9
AC2	−2.6	0.3	0.1	0.4	0.6	1.4	−2.5	−8.5	−0.6	0.8
EJ	−1.2	0.5	0.4	0.7	0.6	2.2	−1.0	−4.9	0.0	0.8
CA1	−1.6	−0.9	0.4	−0.7	0.6	−1.5	−1.7	−5.7	−2.3	0.9
CA2	−1.7	−0.8	0.4	−0.6	0.7	−1.3	−1.6	−5.7	−2.2	1.0
CA3	−1.6	−0.8	0.3	−0.7	0.7	−1.4	−1.6	−5.6	−2.2	0.9
EP1	−0.8	1.0	0.3	1.1	0.8	3.0	−0.8	−5.1	0.4	1.1
EP2	−0.7	1.4	0.4	1.5	0.7	3.8	−0.7	−4.9	0.8	1.0
EP3	−0.8	1.0	0.4	1.1	0.8	3.0	−0.8	−5.1	0.3	1.1
SA	−1.2	0.1	0.4	0.3	0.0	1.4	−1.4	−6.3	−0.2	0.3
LQ1	−0.7	1.3		1.4		3.6	−0.8	−3.3	0.8	
LQ2	−0.8	1.1		1.2		3.3	−0.8	−3.2	0.6	
LQ3	−0.8	1.6		1.8		4.2	−0.8	−3.6	0.9	

values:
$(\delta^{13}C–CO_2)_{MORB}$ = −5‰; $(\delta^{13}C–CO_2)_{Sed}$ = −30‰; $(\delta^{13}C–CO_2)_{Lim}$ = 0‰; $(CO_2/^3He)_{MORB}$ = 1.5 × 10^9; $(CO_2/^3He)_{Sed}$ = 1 × 10^{13}; $(CO_2/^3He)_{Lim}$ = 1 × 10^{13}

According to Eqs. (4) and (5) and *(6)*, the EP, SA and LQ gases were mainly related to decarbonation reactions involving limestone (L: 60–67%), with significant CO_2 contribution from organic-rich sediments (S: 33–40%), whereas mantle CO_2 was almost negligible (M: 0.05–0.2%) (Table 3). It is worth noting that secondary processes, such as multi-step CO_2 dissolution and calcite deposition (Venturi et al., 2017, and references therein), may have modified the carbon isotopic signature of primary biogenic/hydrothermal CO_2, masking the effective contribution of shallow vs. deep CO_2 sources. Hence, the computed percentages of the different CO_2 sources (L, S, and M) must be evaluated with caution.

5.3. Geothermometry

To investigate the chemical-physical conditions at depth of the fluid circulation systems feeding the thermal springs, a theoretical approach based on the chemical equilibria of water-rock reactions involving different mineral phases were considered. As shown by combining the K–Mg and Na–K geothermometers in the Na/400-K/10-√Mg ternary diagram (Giggenbach, 1988, Fig. 8), RE, AC and SA waters plot close to the Mg^{2+} corner, indicating that they were too immature for geothermometer evaluations. CA and EJ waters plot in the partial equilibrium field at < 95 and 140 °C, respectively, whereas significantly higher equilibrium temperatures (> 200 °C) were shown by LQ waters. Eventually, EP waters, although in the immature field, seem to tend to approach partial equilibrium at ~200 °C. In general, none of the water samples appears in full equilibrium conditions, since only CA waters plot very close to the equiline (Fig. 8).

Considering that water chemistry clearly indicates that thermal waters interacted with carbonate-evaporite rocks, a mineral assemblage involving calcite, dolomite, anhydride, fluorite, albite, K-feldspar, Ca- and Mg-saponite (e.g., Benavente et al., 2016) was considered for estimating equilibrium temperatures in the Na^+–K^+–Mg^{2+}–Ca^{2+} system.

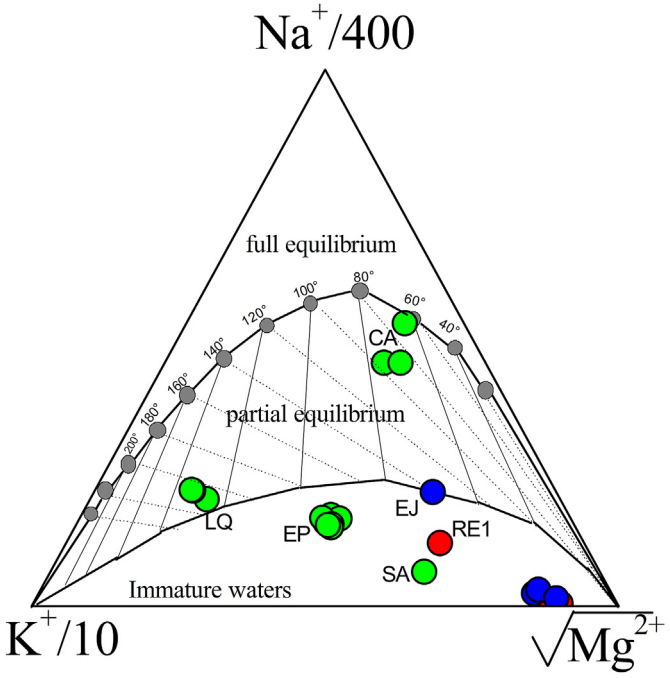

Fig. 8. Mg^{2+}-Na^+-K^+ ternary diagram (modified from Giggenbach, 1988). Partial and full equilibrium curves from 40 to 220 °C are reported. Symbols as in Fig. 1.

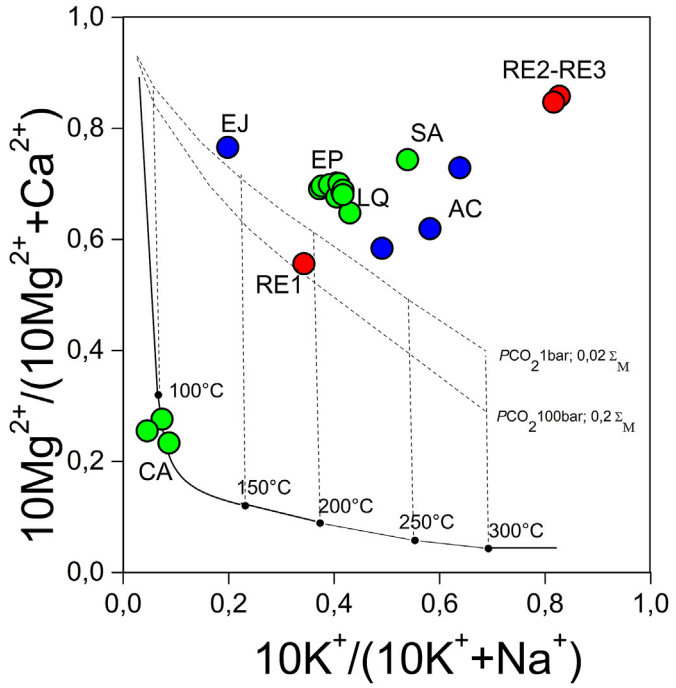

Fig. 9. [10 K^+/(10 K^+ + Na^+)] vs. [10Mg^{2+}/(10Mg^{2+} + Ca^{2+})] binary diagram. Equilibrium curves at temperatures ranging from 100 to 300 °C in presence of different mineral assemblages (Giggenbach, 1988; Chiodini et al., 1995) are reported. Symbols as in Fig. 1.

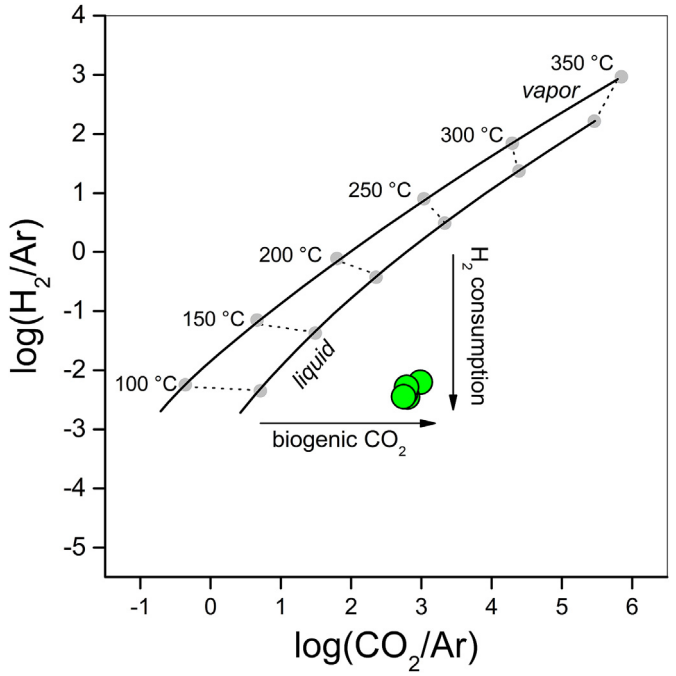

Fig. 10. Log (H_2/Ar) vs. log (CO_2/Ar) binary diagram. Equilibrium curve in liquid and vapor phases at temperatures ranging from 100 to 350 °C and redox conditions controlled by the DP buffer system (D'Amore and Panichi, 1980) are reported. Symbols as in Fig. 1.

Actually, in the (10 K/[10 K + Na] vs. 10 Mg/[10 Mg + Ca]) diagram (Fig. 9), only CA waters plot close the equilibrium curve proposed by Giggenbach (1988), confirming equilibrium temperatures ~100 °C, whereas EJ and EP-LQ waters plot close to the new equilibrium curve computed for low pCO_2 (1 bar) at 140 and 200 °C, respectively. Salta Group sedimentary deposits, which are the most likely hydrothermal

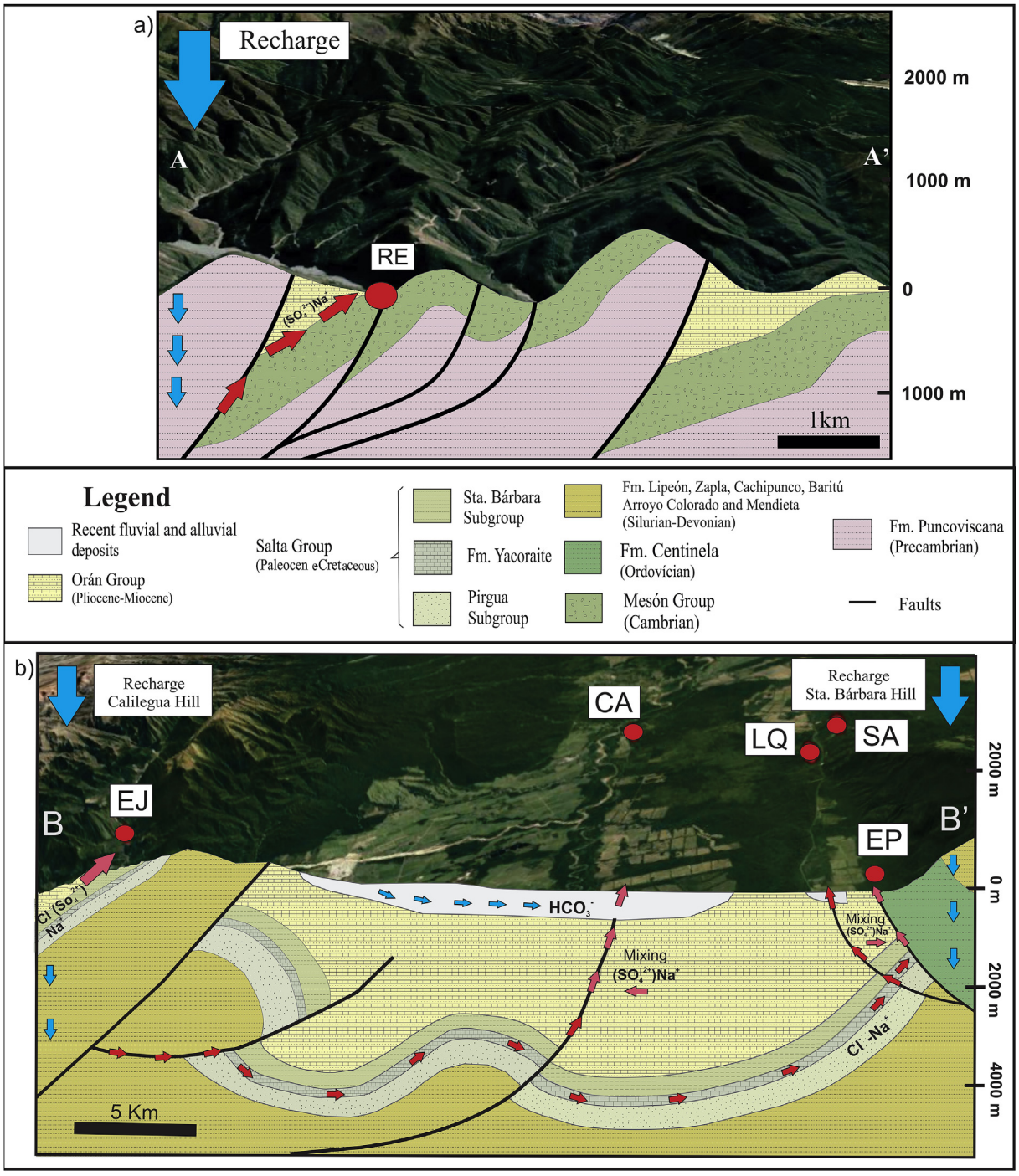

Fig. 11. Conceptual model of the geothermal systems from (a) Termas de Reyes and (b) Subandean Ranges and Santa Barbara System (structural section modified from Kley and Monaldi, 2002)

reservoir feeding EP and LQ springs, in this area locate at a depth > 2000 m. Hence, the relatively high estimated temperatures for these waters suggest the occurrence of an anomalous geothermal gradient in this province, as suggested for other hydrothermal systems in similar geotectonic contexts (Invernizzi et al., 2014; Chiodi et al., 2015; Maffucci et al., 2016). Actually, during the drilling of SA well, upwelling water from ~1000 m depth yielded temperatures higher than 70 °C (Palanca, 1991; Pesce and Miranda, 2003), i.e. almost the double of the expected temperature at that depth under a normal geothermal gradient. Significantly lower temperatures (RE, AC, SA and EJ waters: < 75 °C; CA waters 113–177 °C; EP waters: < 128 °C; LQ waters 138–141 °C) were calculated based on the solubility of chalcedony (Arnorsson, 1983), likely due to the typical dependence of this geothermometer on cooling and dilution commonly affecting uprising thermal fluids. The incomplete maturity of the thermal waters and the lack of significant isotopic shift in the $\delta^{18}O$ values, except for LQ waters (Fig. 3), suggest considering calculated temperatures with severe caution.

Equilibrium temperatures were also tentatively estimated by applying the CO_2–H_2-Ar geothermometers proposed by Giggenbach (1991). Ar concentrations were recalculated by subtracting the respective O_2/22 ratios to prevent the influence of air contamination at the surface, the latter being equal to the minimum Ar concentrations from air contamination since hydrothermal fluids are O_2-free. In the log

(H_2/Ar) vs. (CO_2/Ar) diagram (Fig. 10), at redox conditions controlled by a buffer typical for a hydrothermal system (D'Amore and Panichi, 1980), all bubbling gases plot far from the equilibrium curve in a liquid phase, possibly due to lack of equilibrium of the chemical reactions governing the CO_2 and H_2 concentrations and/or secondary processes occurring at shallow depth, such as H_2 consumption and biogenic CO_2 addition.

6. Conclusions

The chemical and isotopic features of the thermal springs from *EC* and AC waters from *SAR* were related to a shallow hydrological system within a Quaternary and Neogene geological formation and fed by meteoric water infiltrating at > 2500 m a.s.l., likely at the eastern slope of the Chañi hill (West of Reyes thermal springs) (Fig. 11a). Differently, RE1 water likely interacted with Pliocene -Miocene sedimentary units (Orán Group) bearing gypsum deposits (Anta Formation), producing a Na^+-SO_4^{2-} composition after Ca^{2+}-Na^+ exchange with clay minerals. EJ waters from *SAR* were recharged by meteoric water permeating at a relatively low altitude (Fig. 3), likely at the Calilegua Hill (Fig. 1b), that turned to a Cl^-(SO_4^{2-})-Na^+ composition being in contact with Cl- and S-rich evaporite deposits of Orán and Salta groups (Fig. 11b). A similar evolution also characterized LQ thermal springs from SB, where meteoric water from > 2500 m a.s.l., corresponding to Zapla and Calilegua Ranges (Fig. 1b), recharge a mature Na^+-Cl^- hydrothermal reservoir hosted in Yacoraite Formation of the Salta Group. EP, CA and SA waters were the result of mixing the Na^+-Cl^- hydrothermal fluids with shallow, less saline and SO_4^{2-}-dominated aquifers likely hosted in Oran Group (Fig. 11b). Gases within the hydrothermal systems mostly consisted of CO_2 having a crustal origin, mostly deriving from limestone and sediments rich in organic matter, with negligible mantle contribution. Consistently, these gases were characterized by $^3He/^4He$ values between 0.09 and 0.21 Ra. Notwithstanding, hydrothermal waters hosted at great depth (> 2000 m) within the geological units of the Salta Group in the *SB* domain, display a relatively high estimated temperature (~200 °C). These results indicate the occurrence of an anomalous thermal gradient, in agreement with previous studies that investigated different hydrothermal systems in this province (Invernizzi et al., 2014; Chiodi et al., 2015; Maffucci et al., 2016). This work is an additional contribution to the knowledge of the NW Argentine geothermal resource, whose promising results encourage further geological and geophysical surveys in this area, mainly aiming to estimate the effective dimensions and the effective potential of this promising geothermal resource.

7. Author statement

The researchers included in the authors list have had a truly participation during the different work stages, including the elaboration and definition of all aspects of the project (i), the field survey execution (ii), the control of analytical processes and results (iii), the interpretation of the data set (iv), and the elaboration of the manuscript (v) and figures (vi). The role of each researcher is summarized below:

The field survey execution, which included the fluids sampling and the characterization of the local geology and hydrothermal environment was in charge of Y. Peralta Arnold, G. Franco, M., Claros and C. Jofré.

The analytical process was carried out by A. Rizzo and J. Cabassi.

The manuscript preparation was in charge of Y. Peralta Arnold, F. Tassi and G. Franco. P. Caffe, J. Villalba Ulberich and M. Claros especially contributed to the description and interpretation of the geology and tectonic framework of the study region. F. Tassi, A. Rizzo and G. Franco particularly participated in the data interpretation, discussion, and drafting or revision of the manuscript.

The project management manuscript preparation was coordinated by Y. Peralta Arnold who also participated in the elaboration of illustration helped by J. Villalba Ulberich and C. Jofré.

Acknowledgments

Authors thanks the financial support of the Consejo Nacional de Ciencia y Tecnolgía (CONICET, Argentina), Laboratory of Fluid and Rock Geochemistry of the Department of Earth Sciences and CNR-IGG of Florence (Italy). This work was supported by grants PIO-UNJU-CONICET-14020140100010CO, DI-019 DESAFIOS UNJU (Universidad Nacional de Jujuy) and FITR Fonarsec 2013 n. 7 (Agencia Nacional de Promoción Científica y Tecnológica, ANPCyT). We thank the INGV of Palermo for providing analytical support and Mariano Tantillo for the noble gas isotopes measurements. Two anonymous reviewers are greatly acknowledged for their useful comments and suggestions that significantly improved an early version of the manuscript.

References

Aiuppa, A., Avino, R., Brusca, L., Caliro, S., Chiodini, G., D'Alessandro, W., Favara, R., Federico, C., Ginevra, W., Inguaggiato, S., Longo, M., Pecoraino, G., Valenza, M., 2006. Mineral control of arsenic content in thermal waters from volcano-hosted hydrothermal systems: insights from Island of Ischia and Phlegrean Fields (Campanian Volcanic Province, Italy). Chem. Geol. 229, 313–330.

Alcalá, F.J., Custodio, E., 2008. Using the Cl/Br ratio as a natural tracer to identify the origin of salinity in aquifers in Spain and Portugal. J. Hydrol. 359, 198–207.

Aquater, 1980. Exploración geotérmica del área del Cerro Tuzgle, Provincia de Jujuy. Secretaría de Estado de Minería, Argentina (Unpublished report).

Arehart, G.B., Coolbaugh, M.F., Poulson, S.R., 2003. Evidence for a magmatic source of heat for the Steamboat Springs geothermal system using trace elements and gas geochemistry. Trans. Geotherm. Resour. Coun. 269–274.

Arnorsson, S., 1983. Chemical equilibria in Icelandic geothermal systems: implications for chemical geothermometry investigations. Geothermics 12 (2–3), 119–128.

Astini, R.A., 2003. The ordovician proto-Andean basins. Ordovician fossils of Argentina 1, 74.

Baldis, B.A., Gorroño, A., Ploszkiewicz, J.V., Sarudiansky, R.M., 1976. Geotectónica de la Cordillera oriental, sierras subandinas y áreas adyacentes. 1. Sexto Congreso Geológico Argentino, Actas, pp. 3–22 (Bahía Blanca).

Batista Cruz, R.Y., Rizzo, A., Grassa, F., Bernard Romero, R., González Fernández, A., Kretzschmar, T.G., Gómez Arias, E., 2019. Mantle degassing through continental crust triggered by active faults: the case of the baja California peninsula, Mexico. G-cubed 20, 1–25. https://doi.org/10.1029/2018GC007987.

Benavente, O., Tassi, F., Reich, M., Aguilera, F., Capecchiacci, F., Gutiérrez, F., Vaselli, O., Rizzo, A., 2016. Chemical and isotopic features of cold and thermal fluids discharged in the Southern Volcanic Zone between 32.5 S and 36 S: Insights into the physical and chemical processes controlling fluid geochemistry in geothermal systems of Central Chile. Chem. Geol. 420, 97–113.

Bencini, A., 1985. Applicabilità del metodo dell'Azometina-H alla determinazione del Boro nelle acque naturali. Rendiconti della Soc. Ital. Mineral. Petrol. 40, 311–316.

Bencini, A., Martini, M., 1979. Variazioni del contenuto di silice nelle acque freatiche di vulcano. Rendiconti della Soc. Ital. Mineral. Petrol. 35, 639–646.

Bianucci, H., 1973. Informes Mensuales Comisión Geológica N° 3. Yacimientos Petrolíferos Fiscales. (Informe inédito).

Cartwright, I., Weaver, T.R., Fifield, L.K., 2006. Cl/Br ratios and environmental isotopes as indicators of recharge variability and groundwater flow: an example from the southeast Murray Basin, Australia. Chem. Geol. 231 (1–2), 38–56.

Chiodi, A., Tassi, F., Báez, W., Filipovich, R., Bustos, E., Galli, M.G., Suzaño, N., Ahumada, M.F., Viramonte, Giordano, G., Pecorino, G., Vaselli, O., 2019. Preliminary conceptual model of the Cerro Blanco caldera-hosted geothermal system (Southern Puna, Argentina): inferences from geochemical investigations. J. S. Am. Earth Sci. 94, 102213.

Chiodi, A., Tassi, F., Báez, W., Maffucci, R., Invernizzi, C., Giordano, G., Corrado, S., Bicocchi, G., Vaselli, O., Viramonte, J.G., Pierantoni, P.P., 2015. Newgeochemical and isotopic insights to evaluate the geothermal resource of the hydrothermal system of Rosario de la Frontera (Salta, northern Argentina). J. Volcanol. Geoth. Res. 295, 16–25.

Chiodini, G., Frondini, F., Marini, L., 1995. Theoretical geothermometers andPCO2 indicators for aqueous solutions coming from hydrothermal systems of medium-low temperature hosted in carbonate-evaporite rocks. Application to the thermal springs of the Etruscan Swell, Italy. Appl. Geochem. 10 (3), 337–346.

Coira, B., Zappettini, E.O., 2008. Geología y recursos naturales de la Provincia de Jujuy. Relatorio del XVII Congreso Geológico Argentino.

CREGEN, 1988. Estudio geotérmico del área Tuzgle-Tocomar-Pompeya. Centro Regional de Energía Geotérmica (Unpublished report).

D'Amore, F., Panichi, C., 1980. Evaluation of deep temperatures of hydrothermal systems by a new gas geothermometer. Geochem. Cosmochim. Acta 44 (3), 549–556.

Degens, E.T., 1969. Biogeochemistry of stable carbon isotopes. Organic geochemistry. Springer, Berlin, Heidelberg, pp. 304–329.

Disalvo, A., Rodríguez Schelotto, M., Gómez Omil, R., Hoffman, C., Benítez, J., Hurtado, S., 2002. Los reservorios de la Formación Yacoraite. Rocas reservorio de las cuencas productivas de la Argentina. V Congreso de exploración y desarrollo de

hidrocarburos, Mar del Plata, pp. 717–738.
Evans, W.C., White, L.D., Rapp, J.B., 1998. Geochemistry of some gases in hydrothermal fluids from the southern San Juan de Fuca ridge. J. Geophys. Res. 15, 305–313.
Fouillac, C., Michard, G., 1981. Sodium/lithium ratio in water applied to geothermometry of geothermal reservoirs. Geothermics 10 (1), 55–70.
Galli, C.I., Hernández, R., 1999. Evolución de la Cuenca de Antepaís desde la zona de la Cumbre Calchaquí hasta la Sierra de Santa Bárbara, Eoceno inferior-Mioceno medio, provincia de Salta, Argentina. Acta Geol. Hisp. 34 (2), 167–184.
Galli, C.I., Hernández, R.M., Reynolds, J.H., 1996. Análisis paleoambiental y ubicación geocronológica del Subgrupo Metán (Grupo Orán, Neógeno) en el Río Piedras, departamento Metán: Salta, Argentina. Boletín de Informaciones Petroleras. Tercera Época 12, 99–107.
Galliski, M.A., Viramonte, J.G., 1988. The Cretaceous paleorift in northwestern Argentina: a petrologic approach. J. S. Am. Earth Sci. 1 (4), 329–342.
Giggenbach, W., 1988. Geothermal solute equilibria, derivation of Na–K–Mg–Ca geoindicators. Geochem. Cosmochim. Acta 52, 2749–2765.
Giggenbach, W., Goguel, R., 1989. Collection and Analysis of Geothermal and Volcanic Water and Gas Discharges, Unpublished Report. Chemistry Division. Department of Scientific and Industrial Research, Petone, New Zealand, pp. 81.
Giggenbach, W.F., 1991. Chemical techniques in geothermal exploration. In: D'Amore, F. (Ed.), Application of Geochemistry in Geothermal Reservoir Development. UNITAR, pp. 119–144.
Giordano, G., Ahumada, F., Aldega, L., Baez, W., Becchio, R., Bigi, S., Caricchi, C., Chiodi, A., Corrado, S., De Benedetti, A.A., Favetto, A., Fusari, A., Groppelli, G., Invernizzi, C., Maffucci, R., Norini, G., Pinton, A., Pomposiello, C., Tassi, F., Taviani, S., Viramonte, J., 2016. Preliminary data on the structure and potential of the Tocomar geothermal field (Puna plateau, Argentina). Energy Procedia 97, 202–209.
Göb, S., Loges, A., Nolde, N., Bau, M., Jacob, D.E., Markl, G., 2013. Major and trace element compositions (including REE) of mineral, thermal, mine and surface waters in SW Germany and implications for water–rock interaction. Appl. Geochem. 33, 127–152.
Graham, D.W., 2002. Noble gas isotope geochemistry of mid-ocean ridge and ocean island basalts: characterization of mantle source reservoirs. In: Porcelli, D., Ballentine, C.J., Wieler, R. (Eds.), Noble Gases in Geochemistry and Cosmochemistry, Reviews in Mineralogy and Geochemistry. vol. 47. The Mineralogical Society of America, Washington, DC, pp. 245–317.
Harrington, H.J., 1957. 1957 In: Harrington, H.J., Leanza, A.F. (Eds.), Ordovician Trilobites of Argentina. University of Kansas, Special Publication 1, pp. 259.
Heredia, N., Rodríguez Fernández, R., Seggiaro, R.A., González, M.A., 1999. Estructuras de inversión tectónica en la Cordillera Oriental de los Andes, entre 23" y 24" S, Provincia de Jujuy, NO de Argentina. Acta Geol. Hisp. 32 (1–2), 93–101.
Hidroproyectos, S.A., Stec, S.R.L., Sepic, S.C., 1984. Estudio de la segunda fase de prefactibilidad geotérmica del área denominada Tuzgle. Departamento de Susques, Provincia de Jujuy. Ministerio de Economía, dirección de Minería, Jujuy.
Hilton, D.R., Fischer, T.P., Marty, B., 2002. Noble gases and volatile recycling at subduction zones. Rev. Mineral. Geochem. 47, 319–370.
Hoefs, J., 2009. Stable Isotope Chemistry. In: sixth ed. volcanic areas. Rendiconti della Societa Italiana di Mineralogia e Petrologia, vol. 39. Springer, Berlin, New York, pp. 401–405 260.
Hoke, G.D., Aranibar, J.N., Viale, M., Araneo, D.C., Llano, C., 2013. Seasonal moisture sources and the isotopic composition of precipitation, rivers, and carbonates across the Andes at 32.5–35.5 S. G-cubed 14 (4), 962–978.
Invernizzi, C., Pierantoni, P., Chiodi, A., Maffucci, R., Corrado, S., Baez, W., Tassi, F., Giordano, G., Viramonte, J., 2014. Preliminary assessment of the geothermal potential of Rosario de la Frontera area (Salta, NW Argentina): insight from hydrogeological, hydro-geochemical and structural investigations. J. S. Am. Earth Sci. 54, 20–36.
Kaasalainen, H., Stefánsson, A., 2012. The chemistry of trace elements in surface geothermal waters and steam, Iceland. Chem. Geol. 330, 60–85.
Kley, J., Monaldi, C.R., 2002. Tectonic inversion in the Santa Barbara System of the central Andean foreland thrust belt, northwestern Argentina. Tectonics 21 (6), 1061. https://doi.org/10.1029/2002TC902003.
Langelier, W.F., Ludwig, H.F., 1942. Graphical methods for indicating the mineral character of natural waters. J. AWWA (Am. Water Works Assoc.) 34 (3), 335–352.
Lopez Steinmetz, R.L., 2017. Lithium-and boron-bearing brines in the Central Andes: exploring hydrofacies on the eastern Puna plateau between 23° and 23° 30′ S. Miner. Deposita 52 (1), 35–50.
Maffucci, R., Corrado, S., Aldega, L., Bigi, S., Chiodi, A., Di Paolo, L., Giordano, G., Invernizzi, C., 2016. Cap rock efficiency of geothermal systems in fold-and-thrust belts: evidence from paleo-thermal and structural analyses in Rosario de La Frontera geothermal area (NW Argentina). J. Volcanol. Geoth. Res. 328, 84–95.
Mamyrin, B.A., Tolstikhin, I.N., 1984. Helium Isotopes in Nature. Elsevier, Amsterdam.
Marquillas, R.A., Del Papa, C., Sabino, I.F., 2005. Sedimentary aspects and paleoenvironmental evolution of a rift basin: Salta Group (Cretaceous–Paleogene), northwestern Argentina. Int. J. Earth Sci. 94 (1), 94–113.
Martini, M., Cellini Legittimo, P., Piccardi, G., Giannini, L., 1984. Low temperature manifestations in volcanic areas. Rendiconti della Soc. Ital. Mineral. Petrol. 39, 401–405.
McCaffrey, M.A., Lazar, B., Holland, H.D., 1987. The evaporation path of seawater and the coprecipitation of Br- and K+ with halite. J. Sediment. Petrol. 57 (5), 928–937.
Mingramm, A., Russo, A., Pozzo, A., Cazau, L., 1979. Sierras subandinas. In: II Simposio de Geología Regional Argentina, vol. 1. Córdoba, Argentina, pp. 95–138.
Miranda, F., Johanis, P., 2000. Geology and thermal features of El Ramal area, Jujuy province, Argentina. In: Proceedings of the World Geothermal Congress, pp. 1437–1441 Kyushu, Tohoku, Japan.
Monaldi, C.R., Boso, M.A., Fernández, J.C., 1986. Estratigrafía del Ordovícico de la sierra de Zapla, Pcia. Jujuy. Rev. Asoc. Geol. Argent. 41, 62–69.
Moreno Espelta, C., Arias, J.E., Chávez, A., 1978. Geología del Área Termal de Reyes, Departamento Capital, Provincia de Jujuy, República Argentina. 3. Revista del Instituto de Ciencias Geológicas, Universidad Nacional de Jujuy, Jujuy, pp. 161–172.
Ohmoto, H., Goldhaber, M.B., 1997. Sulfur and carbon isotopes. In: Barnes, H.L. (Ed.), Geochemistry of Hydrothermal Ore Deposits. John Wiley & Sons, pp. 517–611.
Ozima, M., Podosek, F.A., 1983. Nobel Gas Geochemistry. Cambridge University Press, Cambridge, UK, pp. 39–41.
Palanca, M.I., 1991. Antecedentes del Termalismo en Jujuy. Publicación de la Universidad Nacional de Jujuy, Serie Arte-Ciencia, pp. 32.
Parkhurst, D.L., Appelo, C.A.J., 1999. User's guide to PHREEQC (version 2)—a computer program for speciation, batch-reaction, one-dimensional transport, and inverse geochemical calculations. U.S. Geo. Surv. Water-Res.ou Invest. Rep. 99–4259, 312.
Peralta Arnold, Y.J., Cabassi, J., Tassi, F., Caffe, J.P., Vaselli, O., 2017. Fluid geochemistry of a deep-seated geothermal resource in the Puna plateau (Jujuy Province, Argentina). J. Volcanol. Geoth. Res. 338, 121–134. https://doi.org/10.1016/j.jvolgeores. 2017.03.030.
Pesce, A., Miranda, F., 2003. Catálogo de manifestaciones termales de la República Argentina. Región Noroeste, Volumen I. SEGEMAR, Buenos Aires, Argentina, pp. 165.
Poreda, R.J., Craig, H., 1989. Helium isotope ratios in circum-Pacific volcanic arcs. Nature 338, 473–478.
Rizzo, A.L., Caracausi, A., Chavagnac, V., Nomikou, P., Polymenakou, P., Mandalakis, M., Kotoulas, G., Magoulas, A., Castillo, A., Lampridou, D., 2016. Kolumbo submarine volcano (Greece): an active window into the Aegean subduction system. Sci. Rep. 6, 28013. https://doi.org/10.1038/srep28013.
Rizzo, A., Barberi, F., Carapezza, M.L., Di Piazza, A., Francalanci, L., Sortino, F., 2015. New mafic magma refilling a quiescent volcano: evidence from He-Ne-Ar isotopes during the 2011-2012 unrest at Santorini, Greece. G-cubed 16 (3), 798–814. https://doi.org/10.1002/2014GC005653.
Rizzo, A.L., Caracausi, A., Chavagnac, V., Nomikou, P., Polymenakou, P.N., Mandalakis, M., Kotoulas, G., Magoulas, A., Castillo, A., Lampridou, D., Marusczak, N., Sonke, J.E., 2019. Geochemistry of CO2-rich gases venting from submarine volcanism: the case of kolumbo (hellenic volcanic arc, Greece). Front. Earth Sci. 7, 60. https://doi.org/10.3389/feart.2019.00060.
Rodríguez Fernández, L.R., Heredia, N., Seggiaro, R.E., González, M., 1999. Estructura andina de la Cordillera Oriental en el área de la Quebrada de Humahuaca, Provincia de Jujuy, NO de Argentina. Trab. Geol. 21, 321–332.
Rollinson, H., 1993. Using Geochemical Data. Longman, London, UK, pp. 352.
Russo, A., 1972. La estratigrafía terciaria en el noroeste argentino. 5° Congreso Geológico Argentino, Villa Carlos Paz, Resúmenes.
Russo, A., Serraiotto, A., 1978. Contribución al conocimiento de la estratigrafía terciaria en el noroeste argentino. In: VII Congreso Geológico Argentino Actas, vol. 1. Neuquén, Argentina, pp. 715–730.
Russo, A., Serraiotto, A., 1979. Contribución al conocimiento de la estratigrafía terciaria en el Noroeste argentino. VII Congreso Geológico Argentino. Actas 1, 505–515.
Salfity, J.A., Marquillas, R.A., 1994. Tectonic and sedimentary evolution of the cretaceous-eocene Salta group basin, Argentina. In: Cretaceous Tectonics of the Andes. Vieweg+ Teubner Verlag, Wiesbaden, pp. 266–315.
Sánchez, M.C., Salfity, J.A., 1999. La cuenca cámbrica del Grupo Mesón en el Noroeste Argentino: desarrollo estratigráfico y paleogeográfico. Acta Geol. Hisp. 34 (2), 123–139.
Sano, Y., Marty, B., 1995. Origin of carbon in fumarolic gases from island arcs. Chem. Geol. 119, 265–274. https://doi.org/10.1016/0009-2541 (94)00097-R.
Schoell, M., 1980. The hydrogen and carbon isotopic composition of methane from natural gases of various origins. Geochem. Cosmochim. Acta 44, 649–661.
Schoell, M., 1988. Multiple origins of methane in the Earth. Chem. Geol. 71, 1–10.
Starck, D., Gallardo, E., Schulz, A., 1993. Neopaleozoic stratigraphy of the sierras Subandinas Orientales and Cordillera Oriental, Argentina. XII Congres International de la Stratigraphie et Geologie du Carbonifere et Permien. Comptes Rendus 2, 353–372.
Tonani, F., 1970. Geochemical methods of exploration for geothermal energy. Geothermics 2, 492–515.
Truesdell, A.H., Hulston, J.R., 1980. Isotopic evidence on environments of geothermal systems. In: Fritz, P. (Ed.), Handbook of Environmental Isotopes Geochemistry. The Terrestrial Environment 1. Elsevier, Amsterdam, pp. 179–226.
Turner, J.C.M., 1959. Estratigrafía del cordón de Escaya y de la sierra de Rinconada (Jujuy). Rev. Asoc. Geol. Argent. 13, 15–39.
Turner, J.C.M., 1960. Estratigrafía de la Sierra de Santa Victoria y adyacencias. Boletín de la Academia Nacional de Ciencias de Córdoba 41 (2), 163–196.
Vaselli, O., Tassi, F., Montegrossi, G., Capaccioni, B., Giannini, L., 2006. Sampling and analysis of volcanic gases. Acta Vulcanol. 18, 65–76.
Venturi, S., Tassi, F., Bicocchi, G., Cabassi, J., Capecchiacci, F., Capasso, G., Vaselli, O., Ricci, A., Grassa, F., 2017. Fractionation processes affecting the stable carbon isotope signature of thermal waters from hydrothermal/volcanic systems: the examples of Campi Flegrei and Vulcano Island (southern Italy). J. Volcanol. Geoth. Res. 345, 46–57.
Whitman, D., Isacks, B.L., Kay, S.M., 1996. Lithospheric structure and along-strike segmentation of the Central Andean Plateau: seismic, magmatism, flexure, topography and tectonics. Tectonophysics 259, 29–40.
Wilhelm, E., Battino, R., Wilcock, R.J., 1977. Low-pressure solubility of gases in liquid water. Chem. Rev. 77, 219–262.
Wilson, N., Webster-Brown, J., Brown, K., 2012. The behaviour of antimony released from surface geothermal features in New Zealand. J. Volcanol. Geoth. Res. 247–248, 158–167.
Carbon isotope fractionation during gas-water exchange and dissolution of CO2. Zhang, J., Quay, P.D., Wilbur, D.O. (Eds.), Geochem. Cosmochim. Acta 59, 107–114.